Specific conformational dynamics of the ATPase head domains and DNA exit gate mediate the Cohesin ATPase cycle

Vitoria Gomes, M.[1,2,3,4,§] , Landwerlin, P.[1,2,3,4,§], Diebold-Durand, M.-L[1,2,3,4,§], Shaik, T.B.[1,2,3,4], Troesch, E.[1,2,3,4], Weber, C.[1,2,3,5], Durand, A.[1,2,3,4], Brillet, K.[6], Dulac, L. [1,2,3,4,5], Antony, P.[1,2,3,4], Watrin, E.[7], Ennifar, E.[6], Golzio, C.[1,2,3,5] and Romier, C.[1,2,3,4,8,*]

[1] Université de Strasbourg, IGBMC UMR 7104- UMR-S 1258, F-67400 Illkirch, France

[2] CNRS, UMR 7104, F-67400 Illkirch, France

[3] Inserm, UMR-S 1258, F-67400 Illkirch, France

[4] IGBMC, Institut de Génétique et de Biologie Moléculaire et Cellulaire, Department of Integrated Structural Biology, F-67400 Illkirch, France

[5] IGBMC, Institut de Génétique et de Biologie Moléculaire et Cellulaire, Department of Translational Medicine and Neurogenetics, F-67400 Illkirch, France

[6] Architecture et Réactivité de l'ARN, Institut de biologie moléculaire et cellulaire (IBMC), UPR 9002 du CNRS, Université de Strasbourg, 15 Rue René Descartes, 67084 Strasbourg Cedex, France.

[7] CNRS, Université de Rennes, Institut de Génétique et Développement de Rennes, UMR 6290, Rennes, France.

[8] Lead contact. romier@igbmc.fr.

[§]These authors have contributed equally to this work.

[*]Correspondence should be addressed to Christophe Romier (romier@igbmc.fr).

Summary

The Cohesin complex is key to eukaryotic genomes organization. ATP binding and hydrolysis are essential to Cohesin functions, but the molecular mechanisms underlying Cohesin ATPase activity remain poorly understood. We characterized distinct steps of the human Cohesin ATPase cycle. Non-engaged SMC1A and SMC3 ATPase domains adopt specific inactive conformations caused by a SMC1A relaxed state and a SMC3/RAD21 DNA exit gate resting state. ATP-dependent ATPase domains engagement leads to a semi-productive ATPase module with a flexible DNA exit gate, and formation of the fully productive ATPase module requires a SMC1A/SMC3 interface reorganization through NIPBL and DNA binding. Functional analyses in zebrafish demonstrate the importance of the full DNA exit gate and its dynamic. The distinct states and concerted movements of Cohesin ATPase domains and DNA exit gate thus mediate the Cohesin ATPase cycle and can be targeted by Cohesin regulators.

Keywords: Genome organization; Chromatin; SMC complexes; ATPase activity; DNA exit gate; Active sites asymmetry; Coiled coils; Conformational changes; Loop extrusion; Resting state.

Introduction

Structural Maintenance of Chromosomes (SMC) complexes play key roles in genome organization in all three kingdoms of life. Accumulating evidence shows that SMC complexes use an ATP-dependent loop extrusion mechanism to perform these roles[1-6]. The various prokaryotic and eukaryotic SMC complexes have, however, evolved different functions that are supported by specific sets of core and regulatory proteins[3,6,7]. How shared and evolutionary-divergent mechanisms of SMC complexes contribute to their specific functions remains poorly understood.

Among the eukaryotic SMC complexes, Cohesin acts in the cohesion of sister chromatids, the segregation of chromosomes, in DNA repair, in V(D)J recombination, in transcription regulation, and in the organization of the genome by forming and maintaining chromatin loops and Topological Associated Domains (TADs)[3,6]. The core Cohesin complex is composed of the SMC1A$^{\mathrm{Smc1}}$ and SMC3$^{\mathrm{Smc3}}$ Smc subunits and of the RAD21$^{\mathrm{Scc1}}$ kleisin subunit (human names used throughout unless species-specific proteins are discussed; *S. cerevisiae* names are hereafter given in superscripts when diverging significantly from the human names). SMC1A and SMC3 subunits harbor at each of their extremities a hinge domain and an ABC-like ATPase head domain (HD), both separated by a long intramolecular coiled coil, while RAD21$^{\mathrm{Scc1}}$ only contains a few folded domains and conserved motifs that are used for interaction with the other Cohesin core and regulatory subunits[6,8,9].

Formation of the Cohesin core complex involves SMC1A and SMC3 heterodimerization through their hinge domains and the asymmetric bridging by the RAD21$^{\mathrm{Scc1}}$ kleisin subunit of SMC1A and SMC3 HDs (Fig. 1A)[10-14]. Specifically, the RAD21$^{\mathrm{Scc1}}$ N-terminal region (RAD21N) is formed of a small helical domain (HelD) followed by a long α-helix. This latter helix interacts with the proximal coiled coil (CC) emerging from the globular domain (GD) of the SMC3 ATPase HD. In contrast, the RAD21$^{\mathrm{Scc1}}$ C-terminal region (RAD21C) folds into a Winged-Helix Domain that directly binds to the GD of the SMC1A HD, thus closing the tripartite ring characteristic of SMC core complexes[10,12]. The DNA-binding STAG1 or STAG2 (SA$^{\mathrm{Scc3}}$) subunit, which is stably associated with the core Cohesin complex and is often considered as its fourth core subunit, plays an important role in the different Cohesin functions, but its precise mode of action still remains elusive[14-28].

The SMC1A and SMC3 HDs also heterodimerize upon binding two ATP molecules in a composite manner to form the Cohesin ATPase module. This latter interaction, known as engagement, is transient and is lost upon ATP hydrolysis. An asymmetry of the Cohesin active sites in the mechanisms underlying genomic cohesion has been reported but remains poorly understood[15,24,29-32]. Cohesin carries out its various functions using ATP-dependent mechanisms, either stably entrapping DNA in a topological manner, or performing loop extrusion to generate chromatin loops by a mechanism that requires pseudo-topological DNA binding[29,30,33-38]. These two activities participate to the Cohesin cycle throughout the cell cycle, synergistically contributing to Cohesin functions and being dependent on the its regulators. Notably, stable association of core Cohesin with DNA initially requires its recruitment to the genome by the MAU2^{Scc4}/NIPBL^{Scc2} complex followed by ATP binding and hydrolysis, leading to topological entrapment[23,32,33,39-42].

Stabilization of Cohesin on the genome further requires acetylation of SMC3 by ESCO1 or ESCO2 (ESCO^{Eco1}) on its K105 and K106 lysine residues (human numbering used throughout), a process requiring ATP-dependent engagement and hydrolysis, and the replacement of NIPBL^{Scc2} by PDS5[27,32,43-51]. While acetylation is sufficient for genomic stabilization of Cohesin in yeast, vertebrate Cohesin additionally requires the action of SORORIN[32,48,52-54]. Unloading of Cohesin from the genome also requires PDS5 when complexed with WAPL and is equally engagement-dependent[15,16,20,24,25,43,48,55-58].

The mechanism of topological DNA entrapment occurs through the SMC1A-hinge/SMC3-hinge interface (DNA entry gate) (Fig. 1A)[38,59,60], although the SMC3 HD/RAD21N interface has also been suggested as an alternative entry gate[24,61]. This latter SMC3 HD/RAD21N interface is generally recognized as the DNA exit gate during G1 and during the prophase[15,24,43,56,59,62], although this interface has also been questioned [63]. In contrast, DNA exit from the Cohesin ring during the anaphase occurs through the proteolytic cleavage of RAD21^{Scc1} by Separase[64-66].

NIPBL^{Scc2} also plays a central role in the Cohesin loop extrusion mechanism, notably through the enhancement of the Cohesin ATPase activity, which is at the core of this mechanism[23,34,37,67]. This stimulation is higher in the presence of DNA although DNA alone barely shows any stimulatory activity. The recent structures of *S. cerevisiae*, *S. pombe* and human Cohesins bound to DNA and to NIPBL^{Scc2} C-terminal region have provided unprecedented information on the intimate interactions of NIPBL^{Scc2}, DNA and the Cohesin ATPase module[14,61,68]. Notably, NIPBL^{Scc2} is favoring HDs engagement, interacting with SMC1A and SMC3 GDs and CCs, these three proteins firmly clamping the DNA between themselves. These structures, which have been obtained in the presence of SMC1A and SMC3 mutants having a low ATP hydrolysis rate, have been described as being in a pre-ATP hydrolysis state that we hereafter term productive state[14,61,68].

Formation of chromatin loops by Cohesin is a highly dynamic and regulated process. Notably, the length of the loops depends not only on NIPBL^{Scc2} and ATP binding and hydrolysis, but also on the action of PDS5, WAPL and SMC3 acetylation and, in vertebrates, of the transcription factor/chromatin insulator CTCF[16,20,22,28,55,57,58,69-78]. Cycles of ATP binding and hydrolysis are crucial, as for other SMC complexes, to the required conformational dynamics of Cohesin[14,18,61,62,68,79-90]. Notably, Cohesin can adopt either an open ring or a rod conformation depending on whether the SMC1A and SMC3 coiled coils are dissociated or interact with each other by co-alignment. In this latter conformation, both SMC1A and SMC3 HDs are in close vicinity, being juxtaposed[81,87].

In contrast, ATP-dependent engagement reorganizes the HDs interface and prevents the SMC1A and SMC3 coiled coils to interact with each other at least in the vicinity of the HDs up to their joint element (Fig. 1A)[14,61,68]. Cohesin coiled coils can also bend at the SMC1A and SMC3 elbow elements, enabling the hinges to come in close vicinity to the HDs[14,61,68,80,87]. How these various conformational movements participate to Cohesin functions is still unclear. A swing-and-clamp mechanism for loop extrusion mediated by the conformational flexibility of Cohesin has however recently been proposed[91]. ATP binding and hydrolysis by Cohesin is therefore key to all Cohesin functions. How this ATPase activity drives the conformational dynamics underlying these functions and how this process is regulated are fundamental questions that require further investigations. Notably, while deciphering the molecular basis of the Cohesin ATPase activity is crucial to understand the structure/function relationships of this complex, our current knowledge on the Cohesin ATPase module remains fragmented. Especially, the precise conformational changes undergone by the SMC1A and SMC3 HDs upon ATP binding, HDs heterodimeric engagement, and ATP hydrolysis are not fully understood.

Here we have characterized the human Cohesin ATPase module by studying the SMC1A and SMC3 HDs independently in their apo, ATP-bound and ADP-bound states, and upon their ATP-dependent engagement. Our study provides the most complete view of the Cohesin ATPase cycle, thus contributing to advance our knowledge of the central mechanisms that underlie Cohesin functions. We notably show that the human SMC1A HD adopts an inactive relaxed conformation and displays a specific conformational dynamic in its different nucleotide binding states. In contrast, human SMC3 is locked in an ATP-hydrolysis inactive state due to a so far uncharacterized resting state adopted by the DNA exit gate. Moreover, a productive conformation of the SMC1A and SMC3 HDs is not fully induced upon HDs engagement but traps the ATPase module in a specific semi-productive state. The fully productive ATPase module formation requires additional structural changes mediated and stabilized by NIPBL^{Scc2} and DNA binding. Our functional analyses in zebrafish further reveal the importance of the full Cohesin DNA exit gate and its dynamic in vertebrates.

Results

Human SMC1A and SMC3 ATPase domains display distinct nucleotide binding properties

To analyze the human Cohesin ATPase module, different constructs of the human SMC1A and SMC3 ATPase head domains (HDs) have been created by varying the length of the proximal coiled coil (CC) emerging from their globular domains (GD). Those included short (SMC1ACCsh), up to the joint element (SMC1ACC and SMC3CC), and including the joint element (SMC1AJ and SMC3J) constructs (Fig. S1A,B). The RAD21N and RAD21C constructs were designed according to previous work (Fig. S1C)[10,12]. Independent expression of the SMC1A, SMC3, RAD21N and RAD21C constructs led to insoluble proteins. However, co-expression of these proteins yielded soluble SMC1A HD/RAD21C and

SMC3 HD/RAD21N complexes. The SMC1ACC/RAD21C and SMC3CC/RAD21N complexes, due to their highest stability, were chosen for our comparative investigations, unless stated.

We first assessed the ATPase activity of the SMC1ACC/RAD21C and SMC3CC/RAD21N complexes, either alone or when mixed together. The independent complexes displayed a very low ATPase activity, but a robust increase in activity was observed upon mixing of the two complexes (Fig. 1B). We next measured the Kd of ADP and ATP for the individual SMC1ACC/RAD21C and SMC3CC/RAD21N complexes using isothermal titration calorimetry (ITC). For ATP, due to the residual ATPase activity of both complexes, Kd measurements were carried out with the wild-type (WT) and with the low ATPase activity EQ mutants (SMC1A-E1157Q and SMC3-E1144Q) as well as with ATP and the low hydrolysable ATPγS analogue.

In the case of ADP, while both complexes displayed a single binding event, the Kd of ADP for SMC1ACC/RAD21C (27.6 µM) was 15 times higher than that for SMC3CC/RAD21N (1.8 µM) (Fig. 1C; Fig. S2A-B; Table S1). In contrast, in the presence of ATP or ATPγS, while the SMC1ACC/RAD21C complex showed a single binding event, the SMC3CC/RAD21N complex unambiguously showed two events (Fig. 1D; Fig. S2A-B). Since ADP binding led to a single event, we reasoned that the second binding event could be due to a homodimerization at high concentration of the SMC3CC/RAD21N complex in the presence of ATP and ATPγS. We therefore processed the ITC data for SMC3 with a model including two consecutive binding events: an initial ATP-binding event followed by a homodimerization event. This model gave a good fitting of the experimental data and yielded one Kd in the µM range and another in the low nM range for the two events (Fig. S2B; Table S1).

Since the measured Kd of ADP for SMC3CC/RAD21N was in the µM range, we assumed that the Kd of ATP and ATPγS for the same complex also corresponded to the higher measured Kd. Comparative analysis of the results obtained showed that both ATP and ATPγS have Kd in a similar range when binding to SMC1ACC/RAD21C and to SMC3CC/RAD21N (Table S1). Nevertheless, major differences were observed when comparing the ITC-measured thermodynamic signatures of the SMC1ACC/RAD21C and SMC3CC/RAD21N complexes binding to ADP, ATP and ATPγS. While the binding reaction to SMC1ACC/RAD21C was entropy-driven, suggesting an increase in solvent entropy, both binding events of SMC3CC/RAD21N were enthalpy-driven (Fig. S2C-D).

A closed conformation of the SMC1A HD P-loop does not prevent nucleotide binding

We next characterized structurally by x-ray crystallography the different complexes purified. Crystallization assays for the SMC1A HD were performed without nucleotide or in the presence of ADP or the low-hydrolysable ATPγS nucleotide. Crystallization attempts for both SMC1ACC/RAD21C and SMC1ACCsh/RAD21C complexes yielded crystals in the three states (apo, ADP-bound and ATPγS-bound) diffracting between 1.36 and 2.50 Å and belonging to different space groups (Tables S2 and S3). In contrast, crystallization attempts with the ATP and ATP-hydrolysis mimics ADP-BeF_3, ADP-AlF_x

and ADP-VO_4 remained unsuccessful. Structure determination was carried out by molecular replacement using the *S. cerevisiae* Smc1 HD/ATPγS structure (PDB entry 1W1W) as model.

Inspection of the electron densities at the nucleotide binding site for the various complexes revealed five binding states: apo, ADP-bound, ADP-Mg-bound, ATPγS-Mg-bound, and a fifth state that we termed loop, where the phosphate loop (P-loop/Walker A motif) was found in two alternative conformations: closed and open. In the apo structures, the P-loop adopts exclusively the closed conformation, which is incompatible with nucleotide binding, while in the nucleotide-bound structures, only the open conformation is observed (Fig. 2A). In the loop structures, both conformations were found, which were most likely caused by the low occupancy binding into the nucleotide-binding pocket of an ion, a cleaved phosphate or a bound ADP or ATPγS molecule.

A closed conformation has also been observed in the *Chaetomium thermophilum* Condensin Smc2 HD, which hampers ATP binding[83]. Our different structures and our ITC results show, however, that the closed conformation in SMC1A cannot prevent nucleotide binding but can potentially set a thermodynamic barrier to this binding. Notably, the closed conformation of the P-loop in human SMC1A is stabilized by a network of water molecules, interacting with neighboring residues (Fig. 2B). Thus, the movement of the P-loop from a closed to an open conformation upon nucleotide binding requires the release of this water network, in agreement with the observed entropy-driven binding of ADP and ATP to SMC1ACC/RAD21C (Fig. S2C). Comparison with the apo structure of *C. thermophilum* Smc1 HD shows that, in this organism, the Smc1 P-loop displays an open conformation[92].

The human SMC1A HD R-loop is poised for nucleotide binding

In its closed conformation, the human SMC1A P-loop is further stabilized by the formation of a larger hydrogen bond network formed between the carbonyl oxygen of S36, the hydroxyl of S39, and the side chains of K13, S14, N40, D43 and R57 (Fig. 2C). The involvement of this latter residue is unexpected since in the fungi Smc1 apo and ATPγS-bound structures, the R-loop, including its arginine residue equivalent to R57, is not observed in density[12,92]. Specifically, ordering of the R-loop only occurs upon the formation of the productive complex in the presence of $\mathrm{NIPBL}^{\mathrm{Scc2}}$ and DNA, suggesting that the R-loop helps sensing the formation of this complex and transmits this information to the ATPase site [68].

In contrast to what is observed in fungi, in all our structures of the human SMC1A HD, the R-loop is defined in density, including the R57 side chain, and the aforementioned hydrogen bond network is conserved in these structures. In the ADP-bound and ATPγS-bound SMC1A HD structures, an additional interaction is formed between the N40 side chain and the sugar of these nucleotides (Fig. 2D). Furthermore, the specific structural rearrangements induced upon ATPγS binding bring the R57 side chain closer to the nucleotide, and the R57 guanidino group also binds to the α phosphate of the nucleotide, still maintaining its interactions with the N40 and D43 side chains (Fig. 2D). These interactions are also observed in the human productive complex, where the R-loop displays a similar conformation to that observed in our structures[14].

To further characterize the role of R57 in the human SMC1A HD, we have either mutated this residue into alanine (R57A) or used the Cornelia de Lange Syndrome (CdLS)-characterized 58-62 deletion mutant (Δ58-62)[93], and analyzed the ability of these mutants to hydrolyze ATP. When investigated on their own, the SMC1ACC-R57A/RAD21C and SMC1ACC-Δ58-62/RAD21C mutants showed no ATP hydrolysis (Fig. 2E). However, the loss of enzymatic activity compared to the WT complex was only ~10% when SMC3CC/RAD21N was added to the reaction. Therefore, in human SMC1A, R57 plays an earlier role in organizing the nucleotide binding site prior to HDs engagement, both by participating to the stabilization of the closed P-loop conformation in the apo state and subsequently by stabilizing ATP binding prior to engagement. This contrasts with the case of fungi Smc1, where the R-loop appears only to play a role once the DNA is bound to the engaged ATPase HDs.

SMC1A HD undergoes specific rotational movements upon binding of nucleotides

We next used our different structures of the SMC1ACC/RAD21C complex to analyze the global structural changes occurring upon ADP and ATP binding. Superposition of the apo and ADP-bound structures, keeping RAD21C as fixed reference, revealed that ADP binding induces rotational movements within the SMC1A HD that are caused by the adjustment of the protein to the bound nucleotide (Fig. 3A). Notably, a rotational movement of the region of the RecA-lobe interacting with the adenine moiety of the ADP molecule is observed toward the RecA-lobe/Helical-lobe interface. In turn, the Helical-lobe is pushed and rotates away from the RecA-lobe (Fig. 3A).

Upon ATPγS-Mg binding, the rotational movement of the RecA-lobe region binding to the adenine moiety toward the RecA-lobe/Helical-lobe interface is conserved and even amplified, notably with the P-loop moving toward this interface compared to what is observed in the ADP-bound structure (Fig. 3B-C). However, in contrast to ADP binding, ATPγS-Mg binding causes the Helical-lobe to move toward the RecA-lobe. This is due to the movement of the Q-loop toward the SMC1A nucleotide binding site, which positions the amide group of the Q137 side chain in productive contact to the Mg ion (1.9 Å) and to the γ group of the ATPγS nucleotide (2.6 Å), a feature that is neither observed in our apo nor in our ADP-bound structures (Fig. 3B-C). These opposite movements of the RecA-lobe and of the Helical-lobe upon ATPγS-Mg binding cause a shrinkage of the SMC1A HD and induce a tightening of the RecA-lobe/Helical-lobe interface. This tightening only induces a few changes in side chain conformations rather than a major reorganization of this interface, and enables the formation of a crystallographic homodimer.

The amplitude of the movements caused by the binding of the nucleotides is larger further away from the nucleotide binding site. This is notably the case of the Helical-lobe that moves essentially as a rigid domain upon ADP and ATPγS binding. Specifically, we observe that the SMC1A CC rotates in opposite directions upon the respective binding of ADP and ATPγS, when compared to a central position of this CC observed in our apo structures, the amplitude of this rotation being larger in the presence of ATPγS (Fig. 3D; Video 1). Importantly, these rotational movements of the CC occur in a same plan that passes through Q137, which explains that this residue reaches in the nucleotide binding site upon ATPγS binding, whereas it moves away from it upon ADP binding (Fig. 3C,E).

Comparative analysis of the *C. thermophilum* apo Smc1 HD with the *S. cerevisiae* Smc1 HD in its ATPγS-bound form, upon keeping Scc1C fixed for superposition, shows similar rotational movements from the apo form to a shrinked ATPγS-bound form, albeit of smaller amplitude (Fig. S3A-B). This is also induced by the movement of the P-loop and of the Q-loop, including a productive interaction of glutamine Q151 with the Mg ion (2.1 Å) and the γ group of the nucleotide (2.9 Å) (Fig. S3C).

SMC1A HD adopts a relaxed conformation regardless of its nucleotide-binding state

We next compared our SMC1ACC/RAD21C structures with that of the SMC1A HD in the productive complex[14], further keeping RAD21C as reference for superposition. This comparison reveals a major movement of the Helical-lobe with respect to the RecA-lobe upon formation of the productive complex (Fig. 4A). This movement, which has been termed lever effect in the bacterial/archeal case[94], does not cause major structural changes within the RecA- and Helical-lobes themselves, but induces a sliding of the Helical-lobe along the RecA-lobe. The amplitude of this movement is very large, as demonstrated by the displacement by ~7-8 Å of the second signature-coupling helix of SMC1A that precedes the N-terminal coil of this HD (Fig. 4A). This large movement occurring upon leverage induces a significant reorganization of the interface between the RecA-lobe and the Helical-lobe of the SMC1A HD.

This sliding movement is almost perpendicular to the aforementioned planar rotational movement observed upon ADP and ATPγS binding to the SMC1A HD, showing that these conformational changes are not related (Fig. 3E and 4A; Video 1). The leverage also repositions the SMC1A CC in a central position, as observed in our apo structure (Fig. 3D and 4B). Despite this central repositioning of the Helical-lobe, the lever effect keeps Q137 at a productive distance to the ATP binding site[14]. While the Helical-lobe overall structure does not change significantly between both structures, we nevertheless observe that the signature motif and the preceding F-loop undergo significant conformational and positional changes upon leverage (Fig. 4C).

Importantly, since neither ADP nor ATPγS binding can induce the productive reorganization of the SMC1A RecA-lobe/Helical-lobe interface in the SMC1ACC/RAD21C complex, we conclude that the SMC1A HD adopts on its own a stable relaxed conformation, regardless of its nucleotide-binding state, which is different from that of the productive state. In the fungi case, a similar relaxed conformation is observed that is not significantly modified upon ATPγS binding. Notably, formation of the fungi productive complex also requires a similar lever effect, even if its amplitude is smaller (~4-5Å) (Fig. S3D-E).

Comparison of our SMC1ACC/RAD21C and SMC1ACCsh/RAD21C structures with that of the productive SMC1A HD reveals that the SMC1ACCsh conformation is closer to that of SMC1A HD in the productive state than in the SMC1ACC/RAD21C complex (Fig. 4A-B). Accordingly, only a small lever effect (1-2 Å) is observed between our SMC1ACCsh/RAD21C structures and the productive SMC1A-HD/RAD21C structure. In agreement, these structures display a similar RecA-lobe/Helical-lobe interface and we also observe a central repositioning of the SMC1ACCsh CC compared to the ATPγS-bound SMC1ACC/RAD21C structure (Fig. 4B).

Inspection of the packing in the crystals of the SMC1ACCsh/RAD21C complex, which is almost identical whatever the nucleotide-binding state, shows however that two symmetry-related complexes interact in a head-to-tail manner in the crystals (Fig. S4). Specifically, the artificial linker built to bridge the two coils of one complex inserts itself into the groove formed between the RecA-lobe and Helical-lobe of the second complex. These artificial interactions favor and stabilize the sliding of both lobes with respect to each other.

Despite their artificial character, the analysis of the SMC1ACCsh/RAD21C structures provide significant information on the SMC1A HD dynamic. Indeed, in the ATPγS-bound SMC1ACCsh/RAD21C structure, Q137 is positioned close but at a non-productive distance to the Mg ion (2.8 Å) and to the γ phosphate of the nucleotide (3.8 Å) (Fig. 4D). Therefore, only the full lever effect can bring Q137 in a productive position. In addition, the F-loop and signature motif are not significantly involved in crystal packing, and no ATP-driven homodimerization of this complex occurs in the SMC1ACCsh/RAD21C crystals. Nevertheless, we observe a conformational and positional changes of the F-loop and signature motif in the SMC1ACCsh/RAD21C structures that are similar to those observed in the productive SMC1A HD/RAD21C structure (Fig. 4C). Thus, the structural and conformational changes undergone by these two functional elements are coupled and are intimately linked to the rearrangements occurring at the RecA-lobe/Helical-lobe interface.

Human SMC3CC/RAD21 is locked into an ATPase inactive state

Crystallization of the human SMC3CC/RAD21N complex was also performed in the absence of any nucleotide or in the presence of ADP, ATPγS as well as ADP-BeF_3, ADP-AlF_x and ADP-VO_4. Crystals belonging to different space groups and diffracting between 2.25 and 3.1 Å were obtained in apo, ADP-bound, ADP-Mg-bound and ATPγS-Mg-bound states (Table S4). Crystals were also obtained with ADP-BeF_3 but diffracted only to 4 Å. Structure determination was carried out by molecular replacement using the yeast Smc3-HD/ATPγS structure (PDB entry 4UX3) as a model. Despite different space groups as well as heterodimerization in the presence of ATPγS and ADP-BeF_3, all structures obtained showed a strong conformational similarity in contrast to what had been observed for SMC1A (Fig. 5A; Video 2). In our structures, the SMC3 R-loop is well defined in density and adopts, as previously observed[10,14,61,68], a different conformation than that of the SMC1A R-loop. Specifically, the SMC3 R57 side chain is exposed at the surface of the SMC3 HD RecA-lobe, being thus poised for interaction with an incoming DNA molecule or any other macromolecule. Similarly, the two lysines K105 and K106, which are targets of the acetylase ESCO^{Eco1}, are also solvent exposed (Fig. 5A). Analysis of the SMC3 nucleotide binding site showed that the P-loop adopts an open conformation in all our structures (Fig. 5B), which may result in the apo structure from the binding of a sulphate ion stemming from the crystallization buffer.

Most importantly, in all our structures the Q-loop is positioned far away (~9 Å) from the nucleotide binding site and the Q141 side chain is turned away from this binding site (Fig. 5B). Comparison of our structures with the structure of the SMC3 HD in the productive complex[14] shows that formation of the productive complex also induces a lever effect that moves the SMC3 second signature-coupling helix by ~4-5 Å (Fig. 5C). The associated conformational changes strongly affect the positioning of the Q-loop in the productive complex, notably with Q141 which is repositioned toward the ATP-binding site (Fig. 5C-D; Video 2).

Moreover, in contrast to our observations on the SMC1A HD, specific additional changes are observed in the SMC3 HD upon formation of the productive complex that are similar to those described upon bacterial/archeal Smc HD homodimerization and leverage[94]. These notably include the conjoint conformational changes in the wedge element and in the R-loop (Fig. 5D). A repositioning but not a conformational rearrangement of the signature motif is also observed between the two structures.

Comparison of the *S. cerevisiae* published Smc3 structures[10,68] shows that a lever effect (6-7 Å) is also required to form the productive state in *S. cerevisiae* (Fig. S5A). The larger lever effect observed for the *S. cerevisiae* Smc3 HD than that for the human SMC3 HD results from a more relaxed conformation of the yeast HD, which also requires a specific conformational rearrangement of the signature motif loop to reach the productive state (Fig. S5B). In addition, a repositioning of the Q-loop is observed between the ATPγS-bound and productive structures of the *S. cerevisiae* Smc3 HD, while it already occurs between the apo and ATPγS-bound states of the fungi Smc1 HD (Fig. S3C and S5A).

The human DNA exit gate in the SMC3CC/RAD21N complex adopts a resting state

Surprisingly, a major specific and unexpected structural feature observed in the human SMC3CC/RAD21N complex is a ~45° kink of the CC emerging from the SMC3 GD compared to the straight conformation displayed by the SMC3 CC in the productive complex (Fig. 6A). This kink is due to a simultaneous bending of both α-helices forming the human SMC3 CC that occurs right above the region where these helices leave the SMC3 GD, and just below the region where they interact with RAD21N (Fig. 6A-B; Video 2).

The flexibility of the short helical stretches of the human SMC3 CC that enables their bending is demonstrated by their two slightly different conformations observed in our different structures, including between non-crystallographic symmetry mates in a single crystal form. These small changes also slightly influence the positioning of the wedge element and, in turn, of the R-loop. This kink is observed in all our SMC3CC/RAD21N structures, regardless of the nucleotide-binding state, the dimerization state and the crystal packing.

Although the folding of RAD21N and its interaction with the CC are not changed by the kink, the new path of the CC positions differently the RAD21N small helical domain (HelD) in the groove at the interface between the SMC3 GD RecA-lobe and Helical-lobe (Fig. 6B). The resulting complex thus stabilizes the DNA exit gate on the SMC3 GD, and we have named resting state this specific conformation of the human SMC3 HD/RAD21N DNA exit gate.

In comparison, in the productive state, the RAD21N HelD is positioned above the SMC3 GD, both domains only forming a single contact through the interaction established between the RAD21N R54 side chain and the SMC3 N123 main chain carbonyl (Fig. 6C-D)[14]. In addition, the productive RAD21N HelD interacts extensively with the bound DNA, both through electrostatic interactions and through direct contacts, such as those that can be formed by RAD21N K25 and K26 with the DNA phosphate backbone (Fig. 6D).

In the resting state, RAD21N residues 5 to 26 pack against the SMC3 GD forming hydrophobic and hydrogen bonding interactions. Notably, the first small α-helix of the RAD21N HelD, composed of residues 13 to 23, packs against the SMC3 RecA-lobe but is also linked to the SMC3 CC through its perpendicular packing interaction with the long α-helix of RAD21N that runs parallel to the SMC3 CC, thus maintaining the structural integrity of the DNA exit gate (Fig. 6B,E).

While residues 13 to 17 of this small helix form main chain/main chain interactions with the SMC3 GD, residues 18 to 23 are involved in main chain/side chain and side chain/side chain interactions with this GD (Fig. 6E). Specifically, tryptophan W18 indole nitrogen makes a pivotal hydrogen bond with the main chain carbonyl of SMC3 S127. Following this helix, RAD21N K25 and K26 side chains interact respectively with the SMC3 GD D120 and D92 side chains. In addition, the R54 guanidino group makes several interactions with the SMC3 GD, notably with the acidic patch formed by the side chains of S131, S133 and D1135 (Fig. 6E).

Strikingly, the position of RAD21N in the resting state is not compatible with the forward movement of the SMC3 second signature-coupling helix occurring upon leverage (Fig. 6F). Therefore, the resting state keeps SMC3 into an inactive conformation by stabilizing the RAD21N HelD on the SMC3 GD and by hampering the structural rearrangements required to reach the productive state. Importantly, our results show that neither ADP nor ATPγS binding are sufficient to release the inactive state of SMC3 imposed by the resting conformation of the DNA exit gate.

Stable engagement of human SMC1A and SMC3 HDs in the presence of ATP

To understand the molecular mechanisms leading to the release of the SMC1A and SMC3 HDs inactive conformations, we have investigated the conformational dynamics of these HDs upon their ATP-dependent engagement. We first looked at conditions favoring stable HDs interaction by using size exclusion chromatography since weakly formed complexes cannot resist the dilution conditions of this technique. Analytical ultracentrifugation velocity measurements were used to confirm the results obtained.

Initial analyses with the WT and EQ constructs revealed that only the SMC1ACC-EQ/RAD21C and the SMC3CC-EQ/RAD21N mutant complexes can stably associate when ATP is present (Fig. 7A-B and S6A). In contrast, combination of WT/WT, WT/EQ and EQ/WT complexes failed to provide a stably engaged ATPase module in the presence of ATP. The fact that RAD21N was not lost in these latter experiments shows that the DNA exit gate remains shut upon engagement and subsequent ATP hydrolysis. Moreover, injection of the two EQ mutants on the ATP-loaded chromatographic column without preincubation with ATP was sufficient to form the complex, demonstrating of its rapid assembly and stability.

In contrast, both size exclusion chromatography and analytical ultracentrifugation showed that while ATP causes engagement, ADP, ATPγS and AMP-PNP cannot (Fig. S6B). In addition, we did not observe a homodimerization of the independent EQ mutants in the presence of ATP, demonstrating of the specificity of the heterodimeric engagement (Fig. S6C). Several signature motif (SMC1A L1128V and SMC3 L1115V) and D-loop (SMC1A D1163E and SMC3 D1150E) mutants have previously been shown, like the EQ mutants, to have a low ATPase activity and to enable engagement[15,29,31]. However, no combination of these mutants yielded stable engagement (Fig. S6D).

Molecular basis of SMC1A and SMC3 HDs engagement

We used our stable engaged ATPase module for structural analyses. Crystallization attempts of the complex only yielded poorly diffracting crystals and cryo-electron microscopy was used instead. Slight crosslinking conditions caused sample aggregation and the purified samples obtained directly from the size exclusion chromatography were therefore used for cryo-EM data collection. Processing of the collected data yielded two cryo-EM maps at 4.0 and 4.5 Å, both representing unambiguously the engaged complex (Fig. S7 and Table S5). While the first map, based on a majority of the particles, was well resolved and used to model the engaged ATPase module, the second map showed more heterogeneity with specific regions not very well defined. This was particularly the case for the SMC1A HD, suggesting that SMC1A can retain some conformational flexibility upon engagement, reminiscent of the higher SMC1A flexibility observed in our crystallographic analyses.

The model of the engaged human Cohesin ATPase module was obtained upon fitting our high-resolution crystallographic structures into the 4.0 Å resolution cryo-EM map, followed by cycles of manual building and automatic real space refinement (Fig. 7C and Table S5). The structure of the engaged human Cohesin ATPase module shows similarities to that bound to NIPBL^{Scc2} and DNA in the productive complex (Fig. 7D). Notably, upon engagement both SMC1A and SMC3 HDs undergo lever effects that release them from their inactive states (Fig. 7E-F). Engagement also repositions both the SMC3 wedge element and the SMC3 R-loop, as seen in the productive complex, showing that these changes are not caused by NIPBL^{Scc2} and DNA binding. As expected, the SMC1A R-loop retains its conformation as observed in the productive but also in the independent SMC1A structures.

Despite these similarities, the structures of the engaged and productive ATPase module show major differences. Indeed, while both SMC1A and SMC3 GDs, when considered independently, exhibit a strong structural similarity in the engaged and productive complexes (Fig. 7E-F), their complex is tighter in the engaged than in the productive state. Notably, when comparing both complexes by superposing one of their HDs, we observe a displacement of the second HD (Fig. 7D). Refinement of the ATPase module taken from the productive complex against our cryo-EM map also resulted in the same tightening, showing that the starting model for structure refinement is not the cause of the difference observed. In addition, this difference was observed when comparing our structure of the engaged module with those of the human, but also of the two yeasts productive complexes [14,61,68].

This difference in the SMC1A/SMC3 GDs interface is mainly caused by the binding of NIPBL^{Scc2} to the engaged complex in the vicinity of the SMC1A F-loop. Indeed, while the F-loop itself is not significantly affected by NIPBL^{Scc2} binding, the insertion of NIPBL^{Scc2} at this SMC1A/SMC3 interface forces both HDs two move apart (Fig. 7D). This movement of both GDs with respect to each other reaches up to the other side of the complex, causing the observed modification of the interface between the SMC1A and SMC3 HDs. This modification does not prevent engagement but alters the interactions between the SMC1A and SMC3 GDs. Notably, the different SMC1A and SMC3 motifs that form both composite ATP binding sites are slightly displaced with respect to each other. These changes are not sufficient to prevent ATP binding but are expected to affect the productive character of both sites.

Notably, in the engaged ATPase module, while the SMC3 site appears poised for hydrolysis, with Q141 now turned toward the active site, the SMC1A active site adopts a non-productive conformation, with SMC1A Q137 which is turned toward the SMC3 signature motif rather than toward the ATP γ-phosphate (Fig.7G-H). In contrast, the glutamines of the SMC1A and SMC3 Q-loops are both turned toward their respective ATP binding site within the yeasts and human productive complexes. Therefore, engagement can occur even if the ATP binding sites are not adopting a full productive organization. Consequently, the ATPase activity at both sites can be regulated, potentially in an independent manner, by slight modifications of the organization of these composite sites.

The other major difference between the engaged and productive ATPase module concerns both SMC1A and SMC3 CCs. In the case of SMC1A, the binding of NIPBL^{Scc2} is responsible for the additional stabilization of 3-5 helical turns within each coil, which corresponds to the interaction region of these coils with NIPBL^{Scc2} hook domain (Fig. 7E). Overall, however, the CC emerging from the SMC1A GD is structurally very similar in both structures, demonstrating of its stability.

In contrast, no density is observed in our cryo-EM map for the DNA exit gate (Fig. 7C). Specifically, the density for the SMC3 CC is lost exactly where this CC is kinked in our crystallographic structures, and no density is observed for RAD21N. This absence of density of the DNA exit gate is already observed at the 2D classification level (Fig. S7) and agrees with the fact that the lever effect is incompatible with the resting state of the DNA exit gate (Fig. 6F). Thus, engagement releases the inactive resting conformation of the DNA exit gate without, however, causing a straightening of the SMC3 CC that would enable the DNA exit gate to adopt a productive conformation (Fig. 7F).

The DNA exit gate becomes flexible upon engagement

To confirm the flexibility of the DNA exit gate observed in our cryo-EM structure, we have performed crosslinking experiments in solution using our SMC1ACC and SMC3CC EQ mutants. Based on our structures and the structure of the productive complex, we identified two pairs of residues in the SMC3 HD and RAD21N (SMC3CC-D120/RAD21N-K25 and SMC3-D92/RAD21N-K26), involving the aforementioned RAD21N K25 and K26 residues (Fig. 6E), that could be crosslinked in the resting state but not in the productive state, when mutated in cysteines. The residues of the first pair were ideally positioned for cross-linking with Bis-maleimidoethane (BMOE) in the resting state (8.5 Å) but not in the productive state (14.0 Å). Those of the second pair were a bit more distant in the resting state (9.5 Å) and very far apart in the productive state (25.0 Å).

Crosslinking of the SMC3CC-D120C/RAD21N-K25C complex gave a robust crosslinking (> 40-50%) at 4°C and room temperature (Fig. 7I and S8A). The amount of crosslink was not significantly modified in the presence of SMC1A, alone or supplemented with either ATP or ATP and DNA. These results therefore confirmed the capacity of the RAD21N to come in close proximity to the SMC3 GD and showed that RAD21N does not dissociate from the SMC3 HD upon ATP-dependent engagement, in agreement with our reconstitution experiments.

The use of the SMC3-D92C/RAD21N-K26C complex also showed a similar crosslinking pattern upon addition of SMC1A. However, additional supplementation of ATP or ATP and DNA caused significant changes in this pattern in a time-dependent manner. This difference is explained by the faster increase of the distance between the SMC3 GD and RAD21N upon movement of the DNA exit gate in the case of this pair. Thus, upon ATP-dependent engagement, the DNA exit gate resting state is released and the gate becomes flexible but neither adopts a stable productive conformation nor opens (Fig. 7J and S8B). This flexibility does not affect the conformation of the SMC3 GD since the position of the SMC3 Helical-lobe is fixed by the HDs engagement and the conformational change of the SMC3 wedge region uncouples the movements of the SMC3 CC to those of the RecA-lobe.

The DNA exit gate and its RAD21N HelD component are functionally important in vertebrates

Our biochemical and structural results suggest a functional role for the human RAD21N HelD. Sequence comparison reveals that this domain is almost fully conserved (sequence identity > 99%) in vertebrates

(Fig. S1C), indicating that the role of the RAD21N HelD should be conserved in these organisms. To assess the functional importance of the RAD21N HelD region in vertebrates, we obtained a characterized *rad21a* zebrafish mutant line[95] which we utilized to evaluate the effect of truncating mutations in these regions. Homozygous larvae exhibited large pericardial edema, microcephaly and curved bodies at 3 days post-fertilization (dpf), which mirrored clinical features of CdLS (Fig. 8A and S9)[96]. These phenotypes were specific and could be rescued efficiently upon injection of 200 pg of WT zebrafish full-length *rad21a* mRNA (Fig. 8A-C and S9).

To test the requirement of the RAD21 HelD domain in Cohesin function, and notably of its N-terminal helix that enables the resting state conformation of the DNA exit gate, we injected a mutant mRNA that did not code for the first 21 amino acids of RAD21 (RAD21-Δ21) into homozygous mutant eggs. The RAD21-Δ21 mRNA failed to rescue the RAD21-/- phenotypes compared to the wild-type mRNA (Fig. 8B-C and S9). Specifically, body curvature, eye diameter (as assessment of the microcephaly) and pericardial edema of RAD21-Δ21-injected larvae were affected indistinguishably from non-injected *rad21a* homozygous mutant larvae. The loss of rescue observed with the RAD21-Δ21 mRNA indicated that the absence of the first 21 residues induces a loss of function of *rad21a*, thus confirming the critical role of the RAD21 HelD domain for Cohesin function in vertebrates.

We made a comparative analysis with a *rad21a* mRNA lacking the full RAD21N region (RAD21-Δ87). This mutant, which should prevent the formation of the Cohesin complex by destroying the DNA exit gate, led to an aggravated phenotype rather than a phenotypic rescue as shown by the presence of necrotic tissues in the head of homozygous mutant embryos at 1 dpf. Similarly, injection of the zebrafish RAD21-Δ87 mRNA into wild-type eggs led to the same severe phenotype suggesting that this truncating mutation acts as a dominant or gain of function allele. Accordingly, acridine orange staining of RAD21-Δ87 mRNA-injected embryos revealed a significant increase in the number of apoptotic cells in the head compared to control embryos or embryos injected with WT *rad21a* mRNA (Fig. 8D). This demonstrates the essential function of RAD21N in vertebrates, including its N-terminal HelD domain.

Discussion

SMC1A and SMC3 HDs undergo specific conformational dynamics during the Cohesin ATPase cycle

The Cohesin ATPase cycle is poorly understood despite its key involvement in the Cohesin functions. Notably, the specific roles of the SMC1A and SMC3 head domains and their dynamic prior, during and after their ATP-dependent engagement have remained elusive. Here we provide the most complete molecular view of the human Cohesin ATPase cycle that reveals the specific dynamics of the SMC1A and SMC3 HDs along the ATPase cycle in support of Cohesin functions (Video 3).

The role and importance of the non-engaged SMC1A and SMC3 HDs are poorly characterized. Inter-species and inter-SMC complexes comparisons did not clearly identify specific conformations that could be mechanistically important. We show here that, on their own, both SMC1A and SMC3 HDs adopt specific inactive conformations whose conformational changes can be regulated. Specifically, ATP binding to the SMC1A HD, which is regulated but not prevented by an initial closed conformation of the SMC1A P-loop, does not release this HD from its relaxed inactive state but induces specific conformational movements that prepare it for engagement. In contrast, ATP binding to the SMC3 HD does not modify its stable resting inactive conformation, which is poised for engagement.

In an open ring conformation of the Cohesin complex, when non-engaged, both HDs are likely to adopt such inactive conformations that can serve as specific docking platforms for Cohesin regulators and partners. Specifically, the observed high flexibility of the regions linking the SMC1A and SMC3 HDs to the Cohesin arms[14,61,68,87] is expected to contribute to the conformational independence of these HDs. Whether HDs juxtaposition upon coiled coils co-alignment can alter SMC1A and SMC3 HDs inactive states remains unknown. We were however unable to stabilize their juxtaposed complex in the absence of ATP in our reconstitution experiments, which suggests a loose association of the HDs upon juxtaposition.

Although both HDs can be relieved from their inactive states through specific lever movements of their Helical-lobes with respect to their RecA-lobes, such conformational changes need to be induced and stabilized to prevent the SMC1A and SMC3 HDs to stay or return to their inactive states. ATP-dependent HDs engagement is sufficient to cause such changes, but the resulting engaged ATPase module only adopts a semi-productive conformation. Additional specific conformational changes of both HDs, caused by NIPBL^{Scc2} and DNA binding, are required to bring the ATPase module in its full productive conformation. Following ATP hydrolysis and disengagement, both HDs return to their inactive states. The higher affinity of the SMC3 HD for ADP than for ATP suggests a potential regulatory step for the next round of engagement.

The semi-productive structure of the engaged ATPase module supports an asymmetry of the Cohesin ATPase active sites

The semi-productive conformation of the engaged ATPase module is due to the specific interface of both SMC1A and SMC3 HDs upon engagement that induces slight conformational changes and repositioning, compared to the productive state, of the motifs (WalkerA/P-loop, Walker B, Q-loop, signature motif, D-loop) that contribute to the composite SMC1A and SMC3 ATPase active sites. Although these small modifications are not sufficient to prevent ATP binding and engagement, they alter the active sites, affecting notably the productive character of the SMC1A active site, but less that of the SMC3 active site. Similar observations on the asymmetry of the Cohesin ATPase active sites have been previously reported by several *in vitro* and *in vivo* studies on yeast and human Cohesins[15,24,29-32].

The characterization of the asymmetry of the Cohesin ATPase active sites stems from the use of several mutants, notably in the Walker B (EQ), signature motif (LV), and D-loop motif (DE) of the SMC1A and SMC3 active sites. These mutants have been shown to display a reduced ATPase activity but to retain engagement. These effects can be explained for the EQ mutant that directly affects the ATPase activity due to the mutation of a major catalytic residue that, however, does not significantly contribute to ATP binding and engagement. This is not the case of the LV and DE mutants whose effect is most likely indirect due to the small structural rearrangements they will cause and that will induce a limited reorganization of the ATP binding site they contribute to. This should perturb the productive character of the active site affected without preventing ATP binding and engagement, similarly to what is observed for the engaged ATPase module.

This fundamental difference between the EQ and LV/DE mutants should however cause the latter mutants to retain a higher residual ATPase activity than the former. Indeed, the intrinsic flexibility that we observe of the engaged ATPase module can induce some remodeling of the active sites over time to lead to metastable productive conformations of these sites. This is assessed by our reconstitution experiments, where the LV and DE mutants cannot stabilize the engaged ATPase module, and by the fact that the LV/DE mutants display milder effects than the EQ mutants *in vivo*[15,29,31]. The same reasoning applies for the requirement of both EQ mutants for the stabilization of the engaged ATPase module in our reconstitution experiments. It has been suggested that, due to this asymmetry, ATP hydrolysis at the SMC3 active site should be sufficient for HDs disengagement[32]. Our structure of the engaged ATPase module supports such a hypothesis, even though a longer residency time of ADP could require further events for disengagement[30].

Molecular basis of Cohesin ATPase activity stimulation by NIPBL^{Scc2} and DNA

The comparative analysis of the structures of the ATPase module in the engaged and productive states reveals the changes induced by NIPBL^{Scc2} and DNA binding to reach the full productive conformation. Those changes go beyond a mere stabilization of the interaction between the SMC1A and SMC3 HDs. Indeed, while engagement causes a lever effect in both HDs, inducing the proper positioning of the SMC3 R-loop for DNA docking and of the SMC1A F-loop for NIPBL^{Scc2} binding, this latter interaction is key in transforming the semi-productive conformation of the engaged ATPase module into its fully productive conformation by reorganizing the interface between the SMC1A and SMC3 GDs.

In addition, NIPBL^{Scc2} binding to SMC1A occurs not only at the F-loop but also at the SMC1A CC, stabilizing additional helical turns of both SMC1A coils upon interaction (Fig. 7E). This double interaction of NIPBL^{Scc2} with the SMC1A F-loop and CC can only occur when the SMC1A Helical-lobe is in a productive conformation since, in the SMC1A relaxed conformation, the F-loop is positioned differently with respect to the CC and adopts a different conformation (Fig. 4C). This implies either that NIPBL^{Scc2} binds to the SMC1A HD when its Helical-lobe is already in a productive conformation, or that NIPBL^{Scc2} causes this lobe to adopt such a productive conformation. Since the productive conformation of the F-loop is linked to the productive interface between the SMC1A RecA-lobe and Helical-lobe, these specific interactions of NIPBL^{Scc2} with the SMC1A Helical-lobe will stabilize the productive conformation of the full SMC1A HD, counteracting the intrinsic flexibility of this HD that we observe in the engaged complex.

The binding of NIPBL^{Scc2} to the engaged ATPase module also contributes to the stabilization of this module, notably through the interaction of the NIPBL^{Scc2} E-loop with both SMC1A and SMC3 GDs (Fig. 7D)[14]. The DNA plays a similar role by docking onto both GDs. These interactions do not cause significant structural changes but certainly favor the full productive conformation of the ATPase module over its semi-productive conformation. In addition, the interaction of the NIPBL^{Scc2} nose domain with the SMC3 joint element further participates to the anchoring of NIPBL^{Scc2} onto the ATPase module but also plays a specific role in stabilizing the DNA exit gate in its productive conformation, which thus also contributes to the stabilization of the rearranged SMC1A GD/SMC3 GD interface. Therefore, NIPBL^{Scc2} and DNA binding to the engaged ATPase module not only favor engagement but induce and stabilize specific conformational changes that transform the semi-productive engaged ATPase module into a full productive complex (Fig. 9).

The DNA exit gate resting state and engagement-induced flexibility can support the swing-and-clamp mechanism for loop extrusion

While the comparative analysis of the engaged and productive ATPase modules reveals the changes occurring upon NIPBL^{Scc2} binding to this complex, they do not inform on how and when this macromolecule docks onto the ATPase module to form the productive complex. Specifically, this docking can initially occur on any of the non-engaged HDs or on the already engaged ATPase module. Interestingly, a swing-and-clamp mechanism as recently been proposed for the formation of the productive complex during loop extrusion by human Cohesin[91]. This mechanism implies an initial spontaneous swinging of the Cohesin arms, upon their bending at their elbow elements, that brings and docks NIPBL^{Scc2}, the SMC1A and SMC3 hinges and the DNA onto the non-engaged SMC3 HD/RAD21N complex. Subsequent engagement/clamping of the HDs then induces conformational changes that release the hinges, while NIPBL^{Scc2} and DNA are repositioned to form the productive complex.

Our analysis of the human Cohesin ATPase cycle shows that the swing-and-clamp mechanism can build on the DNA exit gate resting state and its subsequent engagement-dependent flexibility. Notably, the stable resting conformation of the non-engaged SMC3 HD/RAD21N complex, which is independent of the SMC3 HD nucleotide binding state, can provide a unique stable docking surface for the incoming NIPBL^{Scc2}/hinges/DNA complex. ATP-dependent HDs engagement can then cause the formation of the semi-productive engaged ATPase module, which then releases the resting conformation of the DNA exit gate. The subsequent movement of the DNA exit gate can then enable NIPBL^{Scc2} to bind productively to the engaged ATPase module, bringing in turn this module in its full productive conformation (Fig. 9).

Considering the interaction between the SMC3 joint element and the NIPBL^{Scc2} nose in the productive complex, the NIPBL^{Scc2} nose is likely to interact with the joint element upon docking onto the resting SMC3 HD/RAD21N complex. This could cause the release of the hinges, which have been shown to interact with the NIPBL^{Scc2} nose during the swinging step[91], for a new round of loop extrusion. In addition, the movement of the DNA exit gate can help the Cohesin to alternate between a strong grip on the DNA molecule, in the productive state, and a looser grip, when the DNA exit gate is still oscillating, enabling the DNA to follow the movement of the exit gate and of NIPBL^{Scc2} (Fig. S10A-D).

Specifically, in the productive complex, the DNA is laying on the highly positively charged electrostatic potential of the pit formed by the engaged SMC1A and SMC3 GDs (Fig. S10A). In this complex, the SMC1A CC shows no strong positively or negatively electrostatic potential and appears mainly to act as a rigid wall to maintain the DNA in its binding chamber. In contrast, the DNA exit gate is strongly positively charged, and contributes to the binding of the DNA and to its curvature through electrostatic interactions and direct contacts such as those made by the RAD21N HelD K25 and K26 lysine residues (Fig. S10A-B). In contrast, in a non-productive conformation of the DNA exit gate, the RAD21 HelD is displaced, which widens the DNA binding chamber, easing initial DNA movements and binding (Fig. S10C-D).

How the DNA remains bound to the HDs once the ATP is hydrolyzed and the HDs are disengaged is unclear. In the resting state, however, the RAD21N HelD forms a specific and highly positively charged patch together with the SMC3 GD that is different from that observed when the DNA exit gate is in a productive conformation (Fig. S10E-F). This patch could contribute to maintain DNA binding after disengagement. Juxtaposition of the SMC1A HD with the SMC3 HD and STAG^{Scc3} could also participate to this stabilization of the DNA after disengagement.

Alternative docking modes of NIPBL^{Scc2}

Considering the large interface between NIPBL^{Scc2} and the SMC1A HD in the productive complex, it cannot be excluded that these two macromolecules initially interact together to form this complex. Such a binding could occur prior or after HDs engagement. In the former case, NIPBL^{Scc2} binding can favor the productive conformation of the SMC1A HD, potentially facilitating subsequent ATP binding and engagement with SMC3, while in the latter case, the prior formation of the engaged ATPase module provides a full docking platform for NIPBL^{Scc2}. In these two mechanisms, however, the non-productive conformation of the DNA exit gate appears to hamper its interaction with the NIPBL^{Scc2} nose domain in its productive conformation (Fig. S10G-H).

The formation of the productive complex, when NIPBL^{Scc2} initially binds to the SMC1A HD, would therefore require that both the NIPBL^{Scc2} nose domain and the DNA exit gate move conjointly from initial non-productive conformations to be able to interact as observed in the productive complex. These latter movements could be eased by the reported flexibility of NIPBL^{Scc2} and that we observe for the DNA exit gate[14,19,61,68,97]. The bound DNA could favor this movement by attracting electrostatically the DNA exit gate, notably the HelD. Our crosslinking experiments show however that the interaction of the DNA exit gate with the DNA is not sufficient to stabilize the productive conformation of the gate, implying that the conjoint positioning of NIPBL^{Scc2} onto the DNA is required to stably form the productive complex (Video 3).

Alternatively, it cannot be excluded that initial binding of NIPBL^{Scc2} to the SMC1A HD prevents the interaction between the NIPBL^{Scc2} nose domain and the DNA exit gate. This could yield other interactions between NIPBL^{Scc2} and the ATPase module. Specifically, NIPBL^{Scc2} needs to switch between a loop extrusion mechanism, where the DNA is bound non-topologically, and a genomic loading mechanism, where the DNA is bound topologically. A Cohesin complex where the DNA exit gate remains mobile, as observed in our structure of the engaged ATPase module, could participate to a topological entrapment mechanism.

Potential opening of the DNA exit gate based on the engagement-dependent flexibility of this gate

In agreement, the studies reporting an asymmetry of the Cohesin active sites showed that this difference between the active sites is observed for the NIPBL^{Scc2}-dependent DNA topological entrapment by Cohesin, but also for the ESCO^{Eco1}-mediated SMC3 K105/K106 acetylation and for the PDS5/WAPL-dependent Cohesin genomic unloading[15,24,29-32]. Thus, these different functions, which all require HDs engagement at some stage, could make use of the resting SMC3 HD/RAD21N complex and of the semi-productive ATPase module where the DNA exit gate shows engagement-dependent flexibility (Fig. 9).

Notably, in the case of Cohesin unloading, an engagement-dependent opening of the DNA exit gate is required. Although ATP binding and hydrolysis have been proposed to be sufficient for this opening in the fungi case[92], we do not observe such an opening in our various experiments on the human engaged ATPase module, even with wild-type SMC1A and SMC3 HDs and in conditions where ATP hydrolysis occurs. Interestingly, the region that links the C-terminal extremity of RAD21N to the PDS5 and NIPBL^{Scc2} binding motifs is shorter for the former (~10 residues) than for the latter (~60 residues) (Fig. S1C). This could suggest a potential opening mechanism in the presence of PDS5 and WAPL where the engagement-dependent induced flexibility of the DNA exit gate would exert pulling forces on RAD21N and cause the opening of the DNA exit gate.

The suggested sequestration of the RAD21N HelD by PDS5[48] could further facilitate the exit of the DNA. Interestingly, a role for the RAD21N HelD has also been suggested in the studies reporting DNA topological entrapment through the DNA exit gate[24,61]. In addition, our functional experiments in zebrafish demonstrate of the RAD21N HelD importance in vertebrates. Furthermore, the vicinity of the SMC3 K105 and K106 to the DNA exit gate suggests a modulation of the DNA exit gate dynamics upon recruitment of specific Cohesin regulators by these lysines either acetylated or non-acetylated.

Evolutionary differences of the ATPase module and of the DNA exit gate

The difference in gate opening upon ATP binding/hydrolysis between the fungi and human Cohesin adds to the significant differences highlighted by our study on the HDs and ATPase module from these different organisms. In addition, the RAD21N HelD domain is less conserved at the sequence and structural levels in *S. cerevisiae* Scc1 and several other fungi (Fig. S1C and S11A-D)[10,68], suggesting a specific evolution of this domain in *S. cerevisiae* that could be involved in specific mechanisms. However, whether the *S. cerevisiae* Smc3 CC displays a conformational flexibility, as that we observed for the human SMC3 CC, and that would be mechanistically important, remains to be investigated.

In the case of the *S. pombe* Cohesin, the Rad21N HelD domain structure and position in the productive complex are similar to those of the human RAD21N HelD (Fig. S11E)[61], suggesting that the *S. pombe* SMC3^{Psm3} HD/Rad21N complex could adopt a resting conformation that would potentially be released by ATP-dependent engagement. In line with this observation, the specific crosslinks observed between the *S. pombe* SMC3^{Psm3} HD, Rad21N, NIPBL^{Mis4}, and DNA in the so-called initial binding state compared to the productive/DNA gripping state[61] could correspond to specific interactions occurring upon a docking of NIPBL^{Mis4} and DNA onto a resting SMC3^{Psm3} HD/Rad21N complex, prior to HDs engagement and formation of the DNA gripping complex.

Finaly, the flexibility of the SMC3 CC, which enables the resting state of the DNA exit gate, is observed at the same position in Condensin Smc2, at least in the absence of Brn1N[83,85]. The Brn1N HelD also displays some sequence and structural similarity with that of human RAD21N, including the conservation of a N-terminal helix and of K26 (Brn1 K42; Fig. S11F-G), thus raising the question whether the Condensin DNA exit gate could also adopt a resting state that would be released upon HDs engagement. Specifically, the recent structures of the yeast Condensin ATPase module bound to DNA and to the regulatory subunit Ycs4 show important similarities to the published Cohesin productive complexes[14,61,68,86,88]. Similarly, the reported asymmetry of the Condensin ATPase active sites[98] could also indicate the formation of a semi-productive engaged Condensin ATPase module that would be transformed into a full productive complex upon binding of Ycs4 and DNA.

Conclusions

Collectively, our results reveal the highly dynamic nature of the human Cohesin ATPase cycle that requires specific and concerted conformational movements of the Cohesin ATPase head domains and DNA exit gate. Notably, the Cohesin dynamics cause the HDs to adopt diverse conformations that can modulate the Cohesin ATPase activity and can be the target of the various Cohesin regulators to support the different Cohesin functions (Fig. 9). Understanding how these different conformations and interactions occur throughout the Cohesin cycle will be crucial to further characterize the structure/function relationships of this complex.

Methods

Cloning

The SMC1A and SMC3 ATPase head domain (HD) constructs were generated by PCR using the full length human *smc1a* and *smc3* genes as templates. The sequences coding for the hinges and for the coiled-coils up to the joint elements were replaced by sequences coding for a short protein linker (either ESSKHPASLVPRGS or GSGSLVPRGSGS), as previously reported[10,12]. Point mutations were introduced into the constructions using rolling circle or nested PCR strategies. The constructs were cloned by Gibson assembly into bacterial co-expression vectors[99-102] to code either for native proteins (SMC1A-HD and SMC3-HD constructs) or for proteins followed by a 3C protease cleavage site and a 10xhistidine fusion tag (RAD21N and RAD21C constructs).

Protein complexes production and purification

The same large-scale overproduction and purification methods have been used for all protein complexes, unless stated. The SMC1A or SMC3 HDs-coding plasmids were respectively co-transformed with the RAD21C- or RAD21N-coding plasmids into chemically competent *Escherichia coli* BL21(DE3) cells (Novagen). Co-transformed cells were selected using the appropriate antibiotics. Colonies were used to inoculate large cultures of 2x LB medium that were grown for 6 hours at 37 °C. Protein expression was induced at 25°C by the addition of a final concentration of 0.7 mM Isopropyl β-D-1-thiogalactopyranoside (IPTG; Euromedex), and cells were further grown overnight at 25°C. Culture media was discarded after centrifugation and the bacterial pellets from 3 L of culture were resuspended with 30 ml lysis buffer containing 200 mM or 500 mM NaCl and 10 mM Tris-HCl pH 8. Pellets were stored at -20°C until further use.

After sonication, lysate clarification was performed by centrifugation (1 hour at 17,000 rpm). The recombinant SMC1A HD/RAD21C and SMC3 HD/RAD21N protein complexes were then purified by affinity chromatography using the 10xHis purification tag on RAD21 by incubating the cleared lysates with TALON Metal Affinity Resin (Takara Bio). The purification tag was then removed on the affinity beads by overnight 3C protease digestion at 4°C. Removal of nucleic acid contaminants was performed using 1 ml or 5 ml HiTrap Heparin column (GE Healthcare) and eluted using a NaCl gradient from 50 mM to 1 M. Peak fractions containing the protein complexes were pooled and further purified by size exclusion chromatography using a 16/60 Superdex 200 column (GE Healthcare) equilibrated with a buffer containing 200 mM NaCl, 10 mM Tris-HCl pH 8, 2 mM $MgCl_2$ and either 1 mM TCEP (samples for crystallization and ITC assays) or 2 mM DTT (samples for ATPase assays). The main peak fractions with the protein complexes were pooled, concentrated with AMICON Ultra concentrator filters (Merck Milipore), and either used immediately or frozen in liquid nitrogen and stored at -80°C for later use.

ATPase assays

Measurement of the ATPase activity of wildtype and mutant SMC1A-HD/RAD21C and SMC3-HD/RAD21N complex were assayed using the EnzChek Phosphate Assay Kit (Thermo Fischer Scientific). For these assays, a final concentration of 20 µM of a single protein complex or 10 µM of each protein complex upon mixing were incubated with 1 mM ATP. After addition of ATP, the ATP hydrolysis activity was immediately assessed at 30 °C, by measuring the absorbance at 360 nm every 42 seconds for 2 hours, using a spectrophotometer plate reader (TECAN). The ATPase activities, expressed in Pi molecules released per dimer and per minute shown in the figures were calculated in the linear range of the curves. The experiments have been performed in either duplicates or triplicates.

Isothermal titration calorimetry measurements

For ITC measurements, ATP, ATPγS or ADP were dissolved at a final concentration of 4 mM into the protein gel filtration buffer (200 mM NaCl, 10 mM Tris-HCl pH 8, 2 mM $MgCl_2$ and 1 mM TCEP). Each nucleotide was injected into 189 to 330 µM of either the wildtype or the EQ-mutant SMC1ACC/RAD21C or SMC3CC/RAD21N complexes, respectively. ITC measurements were performed at 5 °C using a PEAQ-ITC microcalorimeter (Malvern Panalytical). ITC data were then corrected for the dilution heats generated by the injection of the buffer into the protein sample and of the nucleotide sample into the buffer. ITC data were then fitted with either one binding event or two binding events models, using the AFFINImeter analysis software.

Cross-linking experiments

For crosslinking experiments, all endogenous cysteines of the SMC1ACC, SMC3CC, RAD21N and RAD21C constructs were mutated into serines to avoid initially observed unspecific crosslinking. The specific cysteines were then introduced in the SMC3CC (D92C and D120C) and RAD21N (K25C or K26C) constructs. All mutated complexes were purified following standard protocol described above. Mutated SMC3CC/RAD21N proteins were mixed to a final concentration of 6 µM alone or in the presence of SMC1ACC/RAD21 (7 µM), ATP (20 µM), DNA (10 µM) and $MgCl_2$ (40 µM). Reactions were incubated for 5 min on ice or at room temperature before addition of 0.5 mM BMOE or DMSO. The reaction was quenched by addition of Laemmli buffer containing β-mercaptoethanol after 2, 5 and 10 minutes, and was further heated at 70°C for 5 min. Samples were loaded on acrylamide gel and band intensity was measured using Fiji[103]. All experiments were performed in triplicates.

Crystallizations

Initial crystallization assays were carried out with commercial crystallization screens in swissci 96-Well 3-Drop MRC crystallization plates (Molecular Dimensions). Crystals were grown using the sitting-drop vapor-diffusion method at 4, 20 and 27 °C. Briefly, 200 nl of 4 to 15 mg/ml protein sample were mixed with 200 nl of reservoir solution. Several conditions from the commercial crystallization screens PACT, JCSG+, Classics, WIZARD I and II, BCS and LFS yielded protein crystals within a few hours up to several weeks. Some of the crystals, especially those from SMC3 HD/RAD21N, required extensive optimization to improve their stability and diffraction limit. Selected crystals were cryo-protected with 20% (v/v) glycerol or 20% (v/v) PEG 200, then flash-cooled and stored into liquid nitrogen until data collection. Crystallization conditions are provided in Tables S2, S3 and S4.

Crystallographic structure determination, model building and refinement

X-ray diffraction data were collected at the SOLEIL and SLS synchrotrons. High resolution diffraction data (ranging from 1.4 to 3.0 Å) were obtained and processed by indexation, integration, and scaling within the XDS program[104]. Data were merged using Aimless from the CCP4 software suite[105]. The various SMC1A HD/RAD21C and SMC3 HD/RAD21N structures were solved by molecular replacement using PhaserMR[106] using respectively the yeast Smc1 HD/Scc1C (PDB entry 1W1W) and Smc3 HD/Scc1N (PDB entry 4UX3) structures as models. The initial models were subsequently iteratively built and refined using the Coot and Phenix refinement programs[107,108]. All refined models were verified with Molprobity[109] and showed good refinement statistics (Tables S2-S4).

Reconstitution of the ATP-engaged ATPase module by size exclusion chromatography

For the characterization of the stably engaged ATPase module by size exclusion chromatography, the WT or EQ independently purified SMC1ACC/RAD21C and SMC3CC/RAD21N complexes were supplemented or not with 0.5/1 mM of the different nucleotides (ADP, ATP, ATPγS, AMP-PNP), diluted to a concentration of 50 µM, and loaded onto a Superdex S200 10/300 column (GE Healthcare) equilibrated with a buffer containing 200 mM NaCl, 10 mM Tris-HCl pH 8.5 mM $MgCl_2$ and 1 mM TCEP, either without nucleotide or supplemented with 0.5/1 mM of the chosen nucleotide. The experiments performed with the WT and EQ, LV and DE mutants were performed initially using the same conditions but incorporating the SMC3J/RAD21N complex instead of the SMC3CC/RAD21N complex.

Reconstitution of the ATP-engaged ATPase module by analytical ultracentrifugation (AUC) experiments

Analytical ultracentrifugation sedimentation velocity experiments were performed with a ProteomeLab® XL (Beckman Coulter) at 4°C and 42,000 rpm with absorbance detection at 280 nm. Independently purified SMC1ACC-EQ/RAD21C and SMC3CC-EQ/RAD21N complexes, stored in a buffer composed of 200 mM NaCl, 10 mM Tris-HCl pH 8.5 mM $MgCl_2$ and 1 mM TCEP, were diluted to a final concentration of 1 mg/mL for experiments with the homodimers or mixed with a 1:0.9 ratio to a final concentration of 1 mg/mL for the heterodimers. ADP, ATP and low-hydrolysable ATP analogs (ATPγS, AMP-PNP) were added to the diluted samples at a concentration of 0.5/1 mM prior to measurements. The A280 nm scans data were acquired at 9 min intervals for 24h. The SEDNTERP software [110] was used to estimate the partial specific volume of the protein (υ), the density (ρ), and the viscosity (η) of the samples. Data were analyzed in the SEDFIT software[111] using the continuous c(s) distribution analysis. AUC graphs were rendered in the GUSSI software[112].

Cryo-electron microscopy sample preparation and data acquisition

For the preparation of the cryo-electron microscopy (cryo-EM) samples, the independently purified SMC1ACC-EQ/RAD21C and SMC3CC-EQ/RAD21N samples were mixed with a 1:0.9 ratio and loaded onto a Superdex 200 16/600 column (GE Healthcare) equilibrated with the purification buffer (200 mM NaCl, 10 mM Tris-HCl pH 8.2 mM $MgCl_2$ and 1 mM TCEP) supplemented with 1 mM ATP. The engaged complex obtained from the most concentrated chromatographic fraction was diluted to 0.3 mg/mL. A 3 µl aliquot of the sample was applied onto an in-house PEGylated gold 1.2/1.3 grid[113]. The grid was blotted for 4s (blot force 5) and flash-frozen in liquid ethane using Vitrobot Mark IV (FEI) at 4°C and 100% humidity. Micrographs were acquired on a Glacios Cryo-TEM operated at 200kV on a K2 Summit camera in counting mode. Automated data acquisition was carried out using the SerialEM software[114] at a 45,000 magnification in a nanoprobe TEM mode, which yielded a pixel size of 0.901 Å. The defocus range was set from -0.8 to -2.0. 40 movies frames were recorded at a dose rate of 7.4 electrons per $Å^2$ per second to a total dose of 44.42 e/$Å^2$. A total of 4146 micrographs were collected.

Cryo-electron microscopy data processing, model building and refinement

The detailed image processing and its related statistics are summarized in Fig. S7. All micrographs were CTF estimated and motion-corrected using Warp[115]. Particles were picked using the neural network BoxNet2 of Warp, yielding 399,773 particles positions. Subsequently, particles were extracted for processing in cryoSPARC[116] to perform 2D classification. 204,379 particles belonging to the best 2D classes were subjected to *ab initio* reconstruction with 2 classes, followed by a non-uniform refinement using default parameters. This refinement on the two classes obtained led to a 4.04 Å map and a 4.50 Å map of the engaged complex. Only the first map, obtained with a majority of the particles, was of sufficient quality for model building.

Model building was performed using our crystal structures of the SMC1ACC/RAD21C, SMC1ACCsh/RAD21C and SMC3CC/RAD21N for docking into the cryo-EM map using UCSF chimera[117]. After few manual adjustments, real-space refinement of the model in Phenix[118] with secondary structure restraints, global minimization, morphing, and simulated annealing was performed. The model was then further improved by several cycles of manual building/adjustment in Coot[108] and real space refinement in Phenix. Model validation was performed within Coot and with MolProbity[119].

Zebrafish rescue experiments and immunostaining

Zebrafish (*Danio rerio*) were raised and maintained as described[120]. The mutant line rad21a$^{hi2529Tg/+}$ (AB genetic background) was obtained from the International Resource Center for Zebrafish (ZIRC#ZDB-ALT-041006-8). The zebrafish line reproduces normally. The *rad21a* heterozygote mutants exhibit no phenotype. The *rad21a* homozygote mutants died at 5 days post-fertilization (dpf) from severe pericardial edema. For this study, viable heterozygous mutant adults were crossed and obtained larvae were individually scored and genotyped following the procedure previously described [95]. All the experiments were at least duplicated, all phenotypes were scored blind to the genotypes, and all statistical analysis were performed using GraphPad Prism v8.0.2.263 (GraphPad Software, San Diego, CA) and R (R Core Team (2021). R: A language and environment for statistical computing. R Foundation for Statistical Computing, Vienna, Austria. URL https://www.R-project.org/).

For wild-type (WT) and mutant rescue experiments, *Danio rerio* WT and truncated *rad21a* messenger RNAs were Sanger sequenced, cloned into pCS2 vector and transcribed using the SP6 mMessage Machine kit (Invitrogen). We injected 200 pg RNA (WT or mutants) into mutant or WT zebrafish embryos at the 1- to 2-cell stage. Eye diameter, body curvature and pericardial edema were scored on injected larvae at 3 dpf fixed in 4% PFA and washed in PBS-Tween 0.1%. Body curvature (Fig. S9A) and eye diameter (Fig. S9B) were measured using Fiji and statistical differences were assessed using ANOVA followed by Turkey's test for post-hoc analysis. For edema scoring, embryos at 3 dpf were classified into three groups: none, mild, and severe based on the size of the edema compared with an age-matched control group from the same clutch (Fig. S9C) and a Fisher's exact test was performed to determine significance.

Acridine orange experiment was performed on embryos at 1dpf. The embryos were dechorionated and incubated at 28°C for 30 min in E3 embryo medium supplemented with 2 µg/mL acridine orange. After extensive washing, embryos were anesthetized with tricaine and imaged as Z-stacks with GFP green light excitation. Cell counting was performed with Fiji using the ITCN plugin. Statistical differences were assessed with a *t*-test. All animal experiments were carried out according to the guidelines of the Ethics Committee of IGBMC and ethical approval was obtained from the French Ministry of Higher Education and Research under the number APAFIS#15025-2018041616344504.

Generation of the graphical supports

The graphics in the figures have been generated with Pymol (The PyMOL Molecular Graphics System, Version 2.0 Schrödinger, LLC), Coot[108], Chimera[117], GraphPad Prism (GraphPad Software, San Diego, CA) and BioRender.com.

Acknowledgments

This work and the authors of this manuscript have been supported by funds from the Fondation ARC (Association pour la Recherche sur le Cancer; ARCPJA20181208268 (CR), ARCPJA2021060003715 (CR) and DOC20180507150 (PL)), from the FRM (Fondation pour la Recherche Médicale; FDT202106012973 (PL)), from the ANR (Agence Nationale de la Recherche; JCJC ANR-17-CE12-0006 (CG)), and by institutional funds from the Centre National de la Recherche Scientifique (CNRS), the Institut National de la Santé et de la Recherche Médicale (INSERM) and the Université de Strasbourg. This work has been published under the framework of the IGBMC INRT Labex (ANR-10-LABX-030-INRT (MVG)), the IdEx Unistra (ANR-10-IDEX-0002 (MLDD, CR)) and the EUR IMCBio (ANR-17-EURE-0023 (MVG)) of the French Investments for the Future Program. The authors acknowledge the support and the use of resources of the French Infrastructure for Integrated Structural Biology (FRISBI; ANR-10-INBS-0005-01) and Instruct-ERIC. The cryo-electron microscope Glacios was co-financed by the European Union, with the European Regional Development Fund (ERDF), the Strasbourg Eurometropole and FRISBI. The cryo-electron microscope Titan was co-financed by FRISBI, the Alsace Region, the General Council of Bas-Rhin and the Ministry of Higher Education and Research. We thank Catherine Birck, Alastair Mc Ewen, Nils Marechal and Pierre Poussin-Courmontagne of the IGBMC Structural Genomics platform for their help during biochemical, biophysical and structural data collection and analysis. We thank Gabor Papai, Nils Marechal and Albert Weixlbaumer for advice on cryo-EM structure refinement. We thank Piotr Sosnowski and Helgo Schmidt for advice with the ATPase assays. We thank the Zebrafish International Resource Center (ZIRC, Oregon, US) for providing the zebrafish line used in this study, and the IGBMC Zebrafish Facility, in particular Sandrine Geschier, for maintenance and care of the zebrafish line. We thank Marianne Lemée for help with Acridine orange experiments on zebrafish and Gaëlle Hayot for help with statistical analyses. We thank members of the SOLEIL and SLS synchrotrons for the use of their beamline facilities and for help during data collection.

Author contributions

MVG, PL, TBS, ET and MLDD made the clones and purified the proteins. MVG and PL performed the ATPase assays. MLDD and MVG performed the crosslinking experiments. KB and EE collected the isothermal titration calorimetry data. MVG, TBS and CR performed the crystallographic analyses. PL, AD, CR and MLDD performed the cryo-EM analyzes. MLDD, CW, LD and CG performed the zebrafish analyzes. MVG, PL, MLDD, TBS, AD, EE, CG and CR planned the experiments. All authors analyzed and discussed the data. CR wrote the manuscript and all authors commented on the manuscript.

Competing financial interests

The authors declare no competing interests.

Figure legends

Figure 1. Distinct ATP hydrolysis and ADP/ATP binding properties of the human SMC1A and SMC3 ATPase head domains.

A. Schematic representation of the human Cohesin core complex. Specific elements are labeled.

B. ATPase activity of the independent and mixed SMC1ACC/RAD21C and SMC3CC/RAD21N complexes. Mixing of both complexes leads to a robust increase in ATPase activity, whereas the independent complexes display very little activity. The ATPase activity is given in Pi molecules released per dimer and per minute.

C. Measurements of the Kd of ADP for the SMC1ACC/RAD21C and SMC3CC/RAD21N complexes. SMC3CC/RAD21N shows a higher affinity for ADP than SMC1ACC/RAD21C.

D. Same as in (C) for ATP. In contrast to ADP, both complexes show a similar Kd for ATP.

Figure 2. Organization of the SMC1A HD ATP binding site by the P-loop and R-loop.

A. Ribbon representation of the SMC1ACC/RAD21C complex in apo, ADP-bound and ATPγS-bound forms upon superposition of the α-helix following the P-loop. In the apo form, the P-loop adopts a closed conformation, whereas it has an open conformation in the nucleotide-bound forms.

B. Interaction network, including water molecules (red spheres), that stabilize the apo closed conformation of the P-loop.

C. Interaction network that stabilizes R57 from the SMC1A R-loop and enables this residue to participate to the organization of the SMC1A ATP binding site already prior to nucleotide binding.

D. Interaction of SMC1A R57 with a bound ATPγS molecule that enable this residue to stabilize nucleotides in the ATP binding site.

E. ATPase activity of the independent (left panel) and SMC3-bound (right panel) SMC1A R57A and CdLS ΔV58-R62 mutants. While the mutations prevent ATP hydrolysis by the independent SMC1A HD, they only slightly affect the ATPase activity of the engaged complex. The ATPase activity is given in Pi molecules released per dimer and per minute.

Figure 3. Specific conformational movements of the SMC1A HD upon nucleotide binding.

A. Conformational movements of the SMC1A HD, keeping RAD21C fixed, upon ADP binding. ADP binding causes rotational movements in the same direction for the RecA-lobe and Helical-lobe.

B. Same as in (A) upon ATPγS and Mg binding. In contrast to ADP binding, the RecA-lobe and Helical lobe of the SMC1A HD rotate in opposite directions upon ATPγS binding, causing a shrinkage of the HD.

C. Specific movements of the SMC1A Q-loop and Q137 depending on the nucleotide binding state. Only ATPγS binding and its associated changes bring Q137 in productive distance to the Mg ion and γ group of the ATPγS molecule.

D. Opposite rotational movements of the SMC1A Helical-lobe upon ADP and ATPγS binding.

E. The movements observed in (D) are in a same plane that passes through Q137, explaining the movements of this catalytic residue in the various nucleotide-binding states.

Figure 4. SMC1A adopts a relaxed conformation different from that in the productive complex.

A. Movements of the Helical-lobe with respect to the RecA-lobe of SMC1A upon formation of the productive complex. These movements are caused by a lever effect which induces a displacement of the CC and a sliding of the second signature-coupling helix of SMC1A. These movements are similar in the SMC1ACCsh which undergoes an artificial lever effect. Therefore, the SMC1A HD adopts a relaxed conformation, regardless of its nucleotide-binding state, which is released by engagement.

B. Same as in (A) in a 90° view focusing on the SMC1A Helical-lobe. A repositioning of the SMC1A CC, like in the apo form, is observed upon the lever effect caused by the formation of the productive complex.

C. Conformational and positional changes occurring in the SMC1A F-loop and signature motif upon formation of the productive complex. These are the only significant changes occurring in the helical lobe and are intimately linked to the reorganization of the RecA-Lobe/Helical-lobe interface as shown by the similar changes observed in the SMC1ACCsh structure that do not homodimerize upon crystallization.

D. The Q-loop and Q137 do not adopt a fully productive position in the SMC1ACCsh/RAD21C structures due to the intermediate lever effect artificially induced on this HD.

Figure 5. SMC3 adopts a stable inactive conformation regardless of its nucleotide-binding state.

A. Superposition of the SMC3CC/RAD21N structures in various nucleotide-binding states (apo, ADP-bound and ATPγS-bound) showing that, in contrast to SMC1A, the SMC3 HD adopts a stable conformation regardless of its nucleotide-binding state.

B. Close-up on the ATP binding site of the structures shown in A. Q141 remains turned away from the active site showing that the SMC3 HD adopts an inactive conformation whatever its nucleotide-binding state.

C. Conformational changes of the SMC3 HD upon formation of the productive complex, including, like for SMC1A, a lever effect that slides the second signature-coupling helix of this HD.

D. Multiple specific changes in the SMC3 HD induced by the formation of the productive complex.

Figure 6. The Cohesin DNA exit gate adopts a stable resting state when the SMC3 HD is non-engaged.

A. Comparison of the independent SMC3 HD structures with that of this HD in the productive complex. A major kink of the SMC3 CC is observed in the non-engaged structures that repositions the RAD21N HelD without perturbing the structure and integrity of the DNA exit gate. We have termed resting state this novel conformation of the DNA exit gate.

B. Structure of the SMC3 HD/RAD21N complex in its resting conformation showing the positioning of the RAD21N HelD domain at the interface between the RecA-lobe and Helical-lobe of the SMC3 HD.

C. Structure of the SMC3 HD/RAD21N complex in its productive conformation showing that the DNA exit gate is further away and hardly interacts with the SMC3 GD.

D. Interactions made by the RAD21N HelD domain with the SMC3 GD and notably the DNA in the productive complex.

E. Interactions made by the RAD21N HelD domain with the SMC3 GD in the resting state.

F. Steric clashes occurring (circle) between the SMC3 second signature-coupling helix in the productive conformation and the RAD21N long α-helix paralleling the SMC3 CC in the resting state. The resting conformation of the DNA exit gate is therefore incompatible with the lever effect in the SMC3 HD.

Figure 7. ATP-dependent engagement of the SMC1A-EQ and SMC3-EQ HDs yields a semi-productive engaged ATPase module with a flexible DNA exit gate.

A. Size exclusion chromatographic profiles and associated SDS-PAGE analyses of the mixed SMC1ACC-EQ/RAD21C and SMC3CC-EQ/RAD21N mutants in the absence (red) and the presence (orange) of ATP. In the presence of ATP, a shift of the peak toward the high molecular weight fractions demonstrates of the stable ATP-dependent engagement of the mutants to form the engaged ATPase module. The fractions analyzed by SDS-PAGE are indicated with a black bar in the chromatographic profiles.

B. Analytical ultracentrifugation velocity experiments confirming that the mutants used in (A) can form the engaged ATPase module in the presence of ATP.

C. Structural model of the human engaged ATPase module displayed within the 4.0 Å resolution cryo-EM map. The map unambiguously shows the absence of a conformationally stable DNA exit gate, implying that, upon engagement, the DNA exit gate is released from its resting state and becomes flexible.

D. Superposition of the engaged and productive ATPase modules using the SMC1A HD as reference for superposition. A displacement of the SMC3 HD with respect to the SMC1A HD is observed between both structures that is due to the binding of NIPBL (blue) to the SMC1A F-loop at the SMC1A/SMC3 interface. For clarity, only the region of NIPBL binding to the F-loop and the NIPBL E-loop are displayed.

E. Superposition of the SMC1A HD in the engaged and productive complexes. Both structures display a very high similarity, showing that engagement already induces most of the conformational changes observed for this HD in the productive complex. The major difference concerns the stabilization of the region of each coil that interacts with the C-terminal part of the hook domain of NIPBL.

F. Superposition of the SMC3 HD in the engaged and productive complexes. Both structures also display a very high similarity, showing that engagement also induces most conformational changes observed in the productive complex. The DNA exit gate composed of the SMC3 CC and RAD21N is however not seen in the engaged ATPase module due to its inherent flexibility and is only stabilized in its productive conformation by the binding of NIPBL and DNA. For simplicity, the SMC3 joint element is not shown.

G. Representation of the motifs forming the SMC1A composite ATPase active site and of the bound ATP molecule embedded in the 4.0 Å cryo-EM map contoured at 5 σ. The active site is in a non-productive mode, notably with SMC1A Q137 which is turned toward and interacts with the SMC3 signature motif.

H. Same as in (G) for the SMC3 composite ATPase active site where the positioning of the different motifs and of Q141 are compatible with productivity.

I. Quantification of crosslinked species for the SMC3CC-D120C/RAD21N-K25C pair in experiments performed at room temperature. The supplementation of the SMC1ACC/RAD21C, ATP and DNA is indicated underneath the graph. Crosslinking of the SMC3 GD and RAD21N is retained even upon ATP-dependent engagement and DNA binding, showing that the exit gate remains shut. All experiments were done in triplicates.

J. Same as in (I) for the SMC3CC-D192C/RAD21N-K26C pair. The longer distance between the SMC3 GD and RAD21N in an extended state of the SMC3 CC enables the observation of the DNA exit gate resting state release and dynamic upon engagement. DNA binding does not alter significantly this dynamic.

Figure 8. Functional importance of the RAD21N HelD domain and of the DNA exit gate in the zebrafish.

A. From left to right, representative lateral images of zebrafish rad21$^{+/+}$ (wildtype; WT), homozygous mutant rad21$^{hi2529Tg/hi2529Tg}$, and homozygous mutant rad21$^{hi2529Tg/hi2529Tg}$ larvae rescued with 200 pg of mRNA encoding WT full-length *Danio rerio rad21* at 3 days post-fertilization (dpf). Scale bar, 0.5 mm. * indicates the presence of a pericardial edema.

B. Dot plots measurements of body curvature (°) and eye diameter (mm) for homozygous mutant rad21$^{hi2529Tg/hi2529Tg}$ larvae injected with sham or full-length WT *Danio rerio rad21a* (RAD21 WT) or with the *rad21a* mRNA lacking the first 21 residues (RAD21-Δ21). Statistical significance was assessed by ANOVA followed by a Tukey's test for post-hoc analysis. All experiments have been performed in biological duplicates. The p-values are indicated on the graphs. N corresponds to the number of embryos per condition.

C. Bar graph showing the presence of pericardial edema for homozygous mutant rad21$^{hi2529Tg/hi2529Tg}$ larvae injected with sham or full-length WT *Danio rerio rad21a* (RAD21 WT) or with the *rad21a* mRNA lacking the first 21 residues (RAD21-Δ21). Larvae were binned into three categories: severe, mild or absent (none). Statistical significance was assessed by a Fisher's exact test. All experiments have been performed in biological duplicates. The p-values are indicated on the graphs. N corresponds to the number of embryos per condition.

D. From left to right, representative lateral images of zebrafish rad21$^{+/+}$ (wildtype; WT) larvae and WT larvae injected with full length WT *Danio rerio rad21* (RAD21 WT) or with the *rad21* mRNA lacking the first 87 residues (RAD21-Δ87) at 1 day post-fertilization and stained with acridine orange to visualize apoptotic cells. The number of apoptotic cells were counted in the highlighted brain area (dotted line on the images). The dot plot represents the number of apoptotic cells/mm^2. A *T*-test was conducted between pairs of conditions to determine significance. The p-values are indicated on the graphs. Acridine orange staining has been performed two times. N corresponds to the number of embryos per condition. Scale bar, 0.1 mm.

Figure 9. Model of ATP-dependent mechanistic pathways underlying the Cohesin functions

Model of the implication of the Cohesin ATPase cycle in the mechanisms supporting the Cohesin functions. The SMC1A and SMC3 HDs are in inactive relaxed and resting conformations prior and after their ATP-dependent engagement. Engagement induces major structural changes in both HDs but leads to a semi-productive conformation of the ATPase module. This semi-productive conformation, which is due to an asymmetry of the SMC1A and SMC3 active sites, could be used by regulators to drive the genomic loading, stabilization and unloading steps of Cohesin. In contrast, this semi-productive conformation is modified by the binding of NIPBL^{Scc2} and DNA to lead to the productive complex involved in loop extrusion. Dissociation of the ATPase module results from ATP hydrolysis at one or both active sites, depending on the conformation of this module. All these mechanisms act synergistically to support the various Cohesin functions.

Video 1. Conformational changes of the SMC1A HD during the ATPase cycle.

Conformational changes undergone by the SMC1A HD upon switching from its apo to its ATP-bound, productive, and ADP-bound states.

Video 2. Conformational changes of the SMC3 HD during the ATPase cycle.

Conformational changes undergone by the SMC3 HD upon switching from its apo to its ATP-bound, productive, and ADP-bound states.

Video 3. Model of the Cohesin ATPase cycle.

Model for the formation of the productive ATPase module of human Cohesin upon docking of NIPBL and DNA onto the semi-productive engaged ATPase module, including a conjoint movement of the NIPBL nose and DNA exit gate. Alternative mechanisms for the formation of the productive complex and the implication of the ATPase module in topological DNA loading and unloading are provided in the discussion.

References

1. Cutts, E.E. & Vannini, A. Condensin complexes: understanding loop extrusion one conformational change at a time. *Biochem Soc Trans* **48**, 2089-2100 (2020).
2. Datta, S., Lecomte, L. & Haering, C.H. Structural insights into DNA loop extrusion by SMC protein complexes. *Curr Opin Struct Biol* **65**, 102-109 (2020).
3. Davidson, I.F. & Peters, J.M. Genome folding through loop extrusion by SMC complexes. *Nat Rev Mol Cell Biol* **22**, 445-464 (2021).
4. Higashi, T.L. & Uhlmann, F. SMC complexes: Lifting the lid on loop extrusion. *Curr Opin Cell Biol* **74**, 13-22 (2022).
5. van Ruiten, M.S. & Rowland, B.D. On the choreography of genome folding: A grand pas de deux of cohesin and CTCF. *Curr Opin Cell Biol* **70**, 84-90 (2021).
6. Yatskevich, S., Rhodes, J. & Nasmyth, K. Organization of Chromosomal DNA by SMC Complexes. *Annu Rev Genet* **53**, 445-482 (2019).
7. Haering, C.H. & Gruber, S. Snapshot: SMC protein complexes Part I. *Cell* **164**, 326 (2016).
8. Gligoris, T. & Lowe, J. Structural Insights into Ring Formation of Cohesin and Related Smc Complexes. *Trends Cell Biol* **26**, 680-693 (2016).
9. Hopfner, K.P. & Tainer, J.A. Rad50/SMC proteins and ABC transporters: unifying concepts from high-resolution structures. *Curr Opin Struct Biol* **13**, 249-55 (2003).
10. Gligoris, T.G. et al. Closing the cohesin ring: structure and function of its Smc3-kleisin interface. *Science* **346**, 963-7 (2014).
11. Haering, C.H., Lowe, J., Hochwagen, A. & Nasmyth, K. Molecular architecture of SMC proteins and the yeast cohesin complex. *Mol Cell* **9**, 773-88 (2002).
12. Haering, C.H. et al. Structure and stability of cohesin's Smc1-kleisin interaction. *Mol Cell* **15**, 951-64 (2004).
13. Kurze, A. et al. A positively charged channel within the Smc1/Smc3 hinge required for sister chromatid cohesion. *EMBO J* **30**, 364-78 (2011).
14. Shi, Z., Gao, H., Bai, X.C. & Yu, H. Cryo-EM structure of the human cohesin-NIPBL-DNA complex. *Science* **368**, 1454-1459 (2020).
15. Beckouet, F. et al. Releasing Activity Disengages Cohesin's Smc3/Scc1 Interface in a Process Blocked by Acetylation. *Mol Cell* **61**, 563-574 (2016).
16. Gandhi, R., Gillespie, P.J. & Hirano, T. Human Wapl is a cohesin-binding protein that promotes sister-chromatid resolution in mitotic prophase. *Curr Biol* **16**, 2406-17 (2006).
17. Hara, K. et al. Structure of cohesin subcomplex pinpoints direct shugoshin-Wapl antagonism in centromeric cohesion. *Nat Struct Mol Biol* **21**, 864-70 (2014).
18. Hons, M.T. et al. Topology and structure of an engineered human cohesin complex bound to Pds5B. *Nat Commun* **7**, 12523 (2016).
19. Kikuchi, S., Borek, D.M., Otwinowski, Z., Tomchick, D.R. & Yu, H. Crystal structure of the cohesin loader Scc2 and insight into cohesinopathy. *Proc Natl Acad Sci U S A* **113**, 12444-12449 (2016).
20. Kueng, S. et al. Wapl controls the dynamic association of cohesin with chromatin. *Cell* **127**, 955-67 (2006).
21. Li, Y. et al. Structural basis for Scc3-dependent cohesin recruitment to chromatin. *Elife* **7**(2018).
22. Li, Y. et al. The structural basis for cohesin-CTCF-anchored loops. *Nature* **578**, 472-476 (2020).
23. Murayama, Y. & Uhlmann, F. Biochemical reconstitution of topological DNA binding by the cohesin ring. *Nature* **505**, 367-71 (2014).
24. Murayama, Y. & Uhlmann, F. DNA Entry into and Exit out of the Cohesin Ring by an Interlocking Gate Mechanism. *Cell* **163**, 1628-40 (2015).
25. Ouyang, Z. et al. Structure of the human cohesin inhibitor Wapl. *Proc Natl Acad Sci U S A* **110**, 11355-60 (2013).

26. Roig, M.B. et al. Structure and function of cohesin's Scc3/SA regulatory subunit. *FEBS Lett* **588**, 3692-702 (2014).
27. Rowland, B.D. et al. Building sister chromatid cohesion: smc3 acetylation counteracts an antiestablishment activity. *Mol Cell* **33**, 763-74 (2009).
28. Wutz, G. et al. ESCO1 and CTCF enable formation of long chromatin loops by protecting cohesin(STAG1) from WAPL. *Elife* **9**(2020).
29. Camdere, G., Guacci, V., Stricklin, J. & Koshland, D. The ATPases of cohesin interface with regulators to modulate cohesin-mediated DNA tethering. *Elife* **4**(2015).
30. Camdere, G.O., Carlborg, K.K. & Koshland, D. Intermediate step of cohesin's ATPase cycle allows cohesin to entrap DNA. *Proc Natl Acad Sci U S A* **115**, 9732-9737 (2018).
31. Elbatsh, A.M.O. et al. Cohesin Releases DNA through Asymmetric ATPase-Driven Ring Opening. *Mol Cell* **61**, 575-588 (2016).
32. Ladurner, R. et al. Cohesin's ATPase activity couples cohesin loading onto DNA with Smc3 acetylation. *Curr Biol* **24**, 2228-37 (2014).
33. Arumugam, P. et al. ATP hydrolysis is required for cohesin's association with chromosomes. *Curr Biol* **13**, 1941-53 (2003).
34. Davidson, I.F. et al. DNA loop extrusion by human cohesin. *Science* **366**, 1338-1345 (2019).
35. Golfier, S., Quail, T., Kimura, H. & Brugues, J. Cohesin and condensin extrude DNA loops in a cell cycle-dependent manner. *Elife* **9**(2020).
36. Haering, C.H., Farcas, A.M., Arumugam, P., Metson, J. & Nasmyth, K. The cohesin ring concatenates sister DNA molecules. *Nature* **454**, 297-301 (2008).
37. Kim, Y., Shi, Z., Zhang, H., Finkelstein, I.J. & Yu, H. Human cohesin compacts DNA by loop extrusion. *Science* **366**, 1345-1349 (2019).
38. Srinivasan, M. et al. The Cohesin Ring Uses Its Hinge to Organize DNA Using Non-topological as well as Topological Mechanisms. *Cell* **173**, 1508-1519 e18 (2018).
39. Ciosk, R. et al. Cohesin's binding to chromosomes depends on a separate complex consisting of Scc2 and Scc4 proteins. *Mol Cell* **5**, 243-54 (2000).
40. Hinshaw, S.M., Makrantoni, V., Harrison, S.C. & Marston, A.L. The Kinetochore Receptor for the Cohesin Loading Complex. *Cell* **171**, 72-84 e13 (2017).
41. Hu, B. et al. ATP hydrolysis is required for relocating cohesin from sites occupied by its Scc2/4 loading complex. *Curr Biol* **21**, 12-24 (2011).
42. Weitzer, S., Lehane, C. & Uhlmann, F. A model for ATP hydrolysis-dependent binding of cohesin to DNA. *Curr Biol* **13**, 1930-40 (2003).
43. Chan, K.L. et al. Cohesin's DNA exit gate is distinct from its entrance gate and is regulated by acetylation. *Cell* **150**, 961-74 (2012).
44. Chan, K.L. et al. Pds5 promotes and protects cohesin acetylation. *Proc Natl Acad Sci U S A* **110**, 13020-5 (2013).
45. Heidinger-Pauli, J.M., Onn, I. & Koshland, D. Genetic evidence that the acetylation of the Smc3p subunit of cohesin modulates its ATP-bound state to promote cohesion establishment in Saccharomyces cerevisiae. *Genetics* **185**, 1249-56 (2010).
46. Lee, B.G. et al. Crystal Structure of the Cohesin Gatekeeper Pds5 and in Complex with Kleisin Scc1. *Cell Rep* **14**, 2108-2115 (2016).
47. Muir, K.W. et al. Structure of the Pds5-Scc1 Complex and Implications for Cohesin Function. *Cell Rep* **14**, 2116-2126 (2016).
48. Ouyang, Z., Zheng, G., Tomchick, D.R., Luo, X. & Yu, H. Structural Basis and IP6 Requirement for Pds5-Dependent Cohesin Dynamics. *Mol Cell* **62**, 248-259 (2016).
49. Rolef Ben-Shahar, T. et al. Eco1-dependent cohesin acetylation during establishment of sister chromatid cohesion. *Science* **321**, 563-6 (2008).
50. Unal, E. et al. A molecular determinant for the establishment of sister chromatid cohesion. *Science* **321**, 566-9 (2008).
51. Zhang, J. et al. Acetylation of Smc3 by Eco1 is required for S phase sister chromatid cohesion in both human and yeast. *Mol Cell* **31**, 143-51 (2008).

52. Ladurner, R. et al. Sororin actively maintains sister chromatid cohesion. *EMBO J* **35**, 635-53 (2016).
53. Lafont, A.L., Song, J. & Rankin, S. Sororin cooperates with the acetyltransferase Eco2 to ensure DNA replication-dependent sister chromatid cohesion. *Proc Natl Acad Sci U S A* **107**, 20364-9 (2010).
54. Nishiyama, T. et al. Sororin mediates sister chromatid cohesion by antagonizing Wapl. *Cell* **143**, 737-49 (2010).
55. Bernard, P. et al. Cell-cycle regulation of cohesin stability along fission yeast chromosomes. *EMBO J* **27**, 111-21 (2008).
56. Eichinger, C.S., Kurze, A., Oliveira, R.A. & Nasmyth, K. Disengaging the Smc3/kleisin interface releases cohesin from Drosophila chromosomes during interphase and mitosis. *EMBO J* **32**, 656-65 (2013).
57. Sutani, T., Kawaguchi, T., Kanno, R., Itoh, T. & Shirahige, K. Budding yeast Wpl1(Rad61)-Pds5 complex counteracts sister chromatid cohesion-establishing reaction. *Curr Biol* **19**, 492-7 (2009).
58. Tedeschi, A. et al. Wapl is an essential regulator of chromatin structure and chromosome segregation. *Nature* **501**, 564-8 (2013).
59. Buheitel, J. & Stemmann, O. Prophase pathway-dependent removal of cohesin from human chromosomes requires opening of the Smc3-Scc1 gate. *EMBO J* **32**, 666-76 (2013).
60. Gruber, S. et al. Evidence that loading of cohesin onto chromosomes involves opening of its SMC hinge. *Cell* **127**, 523-37 (2006).
61. Higashi, T.L. et al. A Structure-Based Mechanism for DNA Entry into the Cohesin Ring. *Mol Cell* **79**, 917-933 e9 (2020).
62. Huis in 't Veld, P.J. et al. Characterization of a DNA exit gate in the human cohesin ring. *Science* **346**, 968-72 (2014).
63. Guacci, V., Chatterjee, F., Robison, B. & Koshland, D.E. Communication between distinct subunit interfaces of the cohesin complex promotes its topological entrapment of DNA. *Elife* **8**(2019).
64. Hauf, S., Waizenegger, I.C. & Peters, J.M. Cohesin cleavage by separase required for anaphase and cytokinesis in human cells. *Science* **293**, 1320-3 (2001).
65. Lin, Z., Luo, X. & Yu, H. Structural basis of cohesin cleavage by separase. *Nature* **532**, 131-4 (2016).
66. Uhlmann, F., Wernic, D., Poupart, M.A., Koonin, E.V. & Nasmyth, K. Cleavage of cohesin by the CD clan protease separin triggers anaphase in yeast. *Cell* **103**, 375-86 (2000).
67. Petela, N.J. et al. Scc2 Is a Potent Activator of Cohesin's ATPase that Promotes Loading by Binding Scc1 without Pds5. *Mol Cell* **70**, 1134-1148 e7 (2018).
68. Collier, J.E. et al. Transport of DNA within cohesin involves clamping on top of engaged heads by Scc2 and entrapment within the ring by Scc3. *Elife* **9**(2020).
69. Dauban, L. et al. Regulation of Cohesin-Mediated Chromosome Folding by Eco1 and Other Partners. *Mol Cell* **77**, 1279-1293 e4 (2020).
70. Feytout, A., Vaur, S., Genier, S., Vazquez, S. & Javerzat, J.P. Psm3 acetylation on conserved lysine residues is dispensable for viability in fission yeast but contributes to Eso1-mediated sister chromatid cohesion by antagonizing Wpl1. *Mol Cell Biol* **31**, 1771-86 (2011).
71. Haarhuis, J.H.I. et al. The Cohesin Release Factor WAPL Restricts Chromatin Loop Extension. *Cell* **169**, 693-707 e14 (2017).
72. Kanke, M., Tahara, E., Huis In't Veld, P.J. & Nishiyama, T. Cohesin acetylation and Wapl-Pds5 oppositely regulate translocation of cohesin along DNA. *EMBO J* **35**, 2686-2698 (2016).
73. Nora, E.P. et al. Molecular basis of CTCF binding polarity in genome folding. *Nat Commun* **11**, 5612 (2020).
74. Rao, S.S.P. et al. Cohesin Loss Eliminates All Loop Domains. *Cell* **171**, 305-320 e24 (2017).
75. Schwarzer, W. et al. Two independent modes of chromatin organization revealed by cohesin removal. *Nature* **551**, 51-56 (2017).

76. Srinivasan, M. et al. Scc2 counteracts a Wapl-independent mechanism that releases cohesin from chromosomes during G1. *Elife* **8**(2019).
77. Vian, L. et al. The Energetics and Physiological Impact of Cohesin Extrusion. *Cell* **175**, 292-294 (2018).
78. Wutz, G. et al. Topologically associating domains and chromatin loops depend on cohesin and are regulated by CTCF, WAPL, and PDS5 proteins. *EMBO J* **36**, 3573-3599 (2017).
79. Anderson, D.E., Losada, A., Erickson, H.P. & Hirano, T. Condensin and cohesin display different arm conformations with characteristic hinge angles. *J Cell Biol* **156**, 419-24 (2002).
80. Burmann, F. et al. A folded conformation of MukBEF and cohesin. *Nat Struct Mol Biol* **26**, 227-236 (2019).
81. Chapard, C., Jones, R., van Oepen, T., Scheinost, J.C. & Nasmyth, K. Sister DNA Entrapment between Juxtaposed Smc Heads and Kleisin of the Cohesin Complex. *Mol Cell* **75**, 224-237 e5 (2019).
82. Diebold-Durand, M.L. et al. Structure of Full-Length SMC and Rearrangements Required for Chromosome Organization. *Mol Cell* **67**, 334-347 e5 (2017).
83. Hassler, M. et al. Structural Basis of an Asymmetric Condensin ATPase Cycle. *Mol Cell* **74**, 1175-1188 e9 (2019).
84. Kulemzina, I. et al. A Reversible Association between Smc Coiled Coils Is Regulated by Lysine Acetylation and Is Required for Cohesin Association with the DNA. *Mol Cell* **63**, 1044-54 (2016).
85. Lee, B.G. et al. Cryo-EM structures of holo condensin reveal a subunit flip-flop mechanism. *Nat Struct Mol Biol* **27**, 743-751 (2020).
86. Lee, B.G., Rhodes, J. & Lowe, J. Clamping of DNA shuts the condensin neck gate. *Proc Natl Acad Sci U S A* **119**, e2120006119 (2022).
87. Petela, N.J. et al. Folding of cohesin's coiled coil is important for Scc2/4-induced association with chromosomes. *Elife* **10**(2021).
88. Shaltiel, I.A. et al. A hold-and-feed mechanism drives directional DNA loop extrusion by condensin. *Science* **376**, 1087-1094 (2022).
89. Soh, Y.M. et al. Molecular basis for SMC rod formation and its dissolution upon DNA binding. *Mol Cell* **57**, 290-303 (2015).
90. Vazquez Nunez, R., Ruiz Avila, L.B. & Gruber, S. Transient DNA Occupancy of the SMC Interarm Space in Prokaryotic Condensin. *Mol Cell* **75**, 209-223 e6 (2019).
91. Bauer, B.W. et al. Cohesin mediates DNA loop extrusion by a "swing and clamp" mechanism. *Cell* **184**, 5448-5464 e22 (2021).
92. Muir, K.W., Li, Y., Weis, F. & Panne, D. The structure of the cohesin ATPase elucidates the mechanism of SMC-kleisin ring opening. *Nat Struct Mol Biol* **27**, 233-239 (2020).
93. Rohatgi, S. et al. Facial diagnosis of mild and variant CdLS: Insights from a dysmorphologist survey. *Am J Med Genet A* **152A**, 1641-53 (2010).
94. Kamada, K., Su'etsugu, M., Takada, H., Miyata, M. & Hirano, T. Overall Shapes of the SMC-ScpAB Complex Are Determined by Balance between Constraint and Relaxation of Its Structural Parts. *Structure* **25**, 603-616 e4 (2017).
95. Xu, B., Sowa, N., Cardenas, M.E. & Gerton, J.L. L-leucine partially rescues translational and developmental defects associated with zebrafish models of Cornelia de Lange syndrome. *Hum Mol Genet* **24**, 1540-55 (2015).
96. Kline, A.D. et al. Diagnosis and management of Cornelia de Lange syndrome: first international consensus statement. *Nat Rev Genet* (2018).
97. Chao, W.C. et al. Structure of the cohesin loader Scc2. *Nat Commun* **8**, 13952 (2017).
98. Elbatsh, A.M.O. et al. Distinct Roles for Condensin's Two ATPase Sites in Chromosome Condensation. *Mol Cell* **76**, 724-737 e5 (2019).
99. Diebold, M.L., Fribourg, S., Koch, M., Metzger, T. & Romier, C. Deciphering correct strategies for multiprotein complex assembly by co-expression: application to complexes as large as the histone octamer. *J Struct Biol* **175**, 178-88 (2011).

100. Fribourg, S. et al. Dissecting the interaction network of multiprotein complexes by pairwise coexpression of subunits in E. coli. *J Mol Biol* **306**, 363-73 (2001).
101. Romier, C. et al. Co-expression of protein complexes in prokaryotic and eukaryotic hosts: experimental procedures, database tracking and case studies. *Acta Crystallogr D Biol Crystallogr* **62**, 1232-42 (2006).
102. Vincentelli, R. & Romier, C. Complex Reconstitution and Characterization by Combining Co-expression Techniques in Escherichia coli with High-Throughput. *Adv Exp Med Biol* **896**, 43-58 (2016).
103. Schindelin, J. et al. Fiji: an open-source platform for biological-image analysis. *Nature Methods* **9**, 676-682 (2012).
104. Kabsch, W. Xds. *Acta Crystallogr D Biol Crystallogr* **66**, 125-32 (2010).
105. The CCP4 suite: programs for protein crystallography. *Acta Crystallogr D Biol Crystallogr* **50**, 760-3 (1994).
106. McCoy, A.J. et al. Phaser crystallographic software. *J Appl Crystallogr* **40**, 658-674 (2007).
107. Adams, P.D. et al. PHENIX: A comprehensive Python-based system for macromolecular structure solution. *Acta Crystallographica Section D: Biological Crystallography* **66**, 213-221 (2010).
108. Emsley, P., Lohkamp, B., Scott, W.G. & Cowtan, K. Features and development of Coot. *Acta Crystallographica Section D: Biological Crystallography* **66**, 486-501 (2010).
109. Williams, C.J. et al. MolProbity: More and better reference data for improved all-atom structure validation. *Protein Sci* **27**, 293-315 (2018).
110. Laue, T.M., Shah, B.D., Ridgeway, T.M., Pelletier, S.L. *Computer-aided Interpretation of Sedimentation Data for Proteins*, (Royal Society of Chemistry, Cambridge [England], 1992).
111. Schuck, P. Size-distribution analysis of macromolecules by sedimentation velocity ultracentrifugation and lamm equation modeling. *Biophys J* **78**, 1606-19 (2000).
112. Brautigam, C.A. Calculations and Publication-Quality Illustrations for Analytical Ultracentrifugation Data. *Methods Enzymol* **562**, 109-33 (2015).
113. Meyerson, J.R. et al. Self-assembled monolayers improve protein distribution on holey carbon cryo-EM supports. *Sci Rep* **4**, 7084 (2014).
114. Mastronarde, D.N. Automated electron microscope tomography using robust prediction of specimen movements. *J Struct Biol* **152**, 36-51 (2005).
115. Tegunov, D. & Cramer, P. Real-time cryo-electron microscopy data preprocessing with Warp. *Nat Methods* **16**, 1146-1152 (2019).
116. Punjani, A., Zhang, H. & Fleet, D.J. Non-uniform refinement: adaptive regularization improves single-particle cryo-EM reconstruction. *Nat Methods* **17**, 1214-1221 (2020).
117. Pettersen, E.F. et al. UCSF Chimera--a visualization system for exploratory research and analysis. *J Comput Chem* **25**, 1605-12 (2004).
118. Liebschner, D. et al. Macromolecular structure determination using X-rays, neutrons and electrons: recent developments in Phenix. *Acta Crystallogr D Struct Biol* **75**, 861-877 (2019).
119. Prisant, M.G., Williams, C.J., Chen, V.B., Richardson, J.S. & Richardson, D.C. New tools in MolProbity validation: CaBLAM for CryoEM backbone, UnDowser to rethink "waters," and NGL Viewer to recapture online 3D graphics. *Protein Sci* **29**, 315-329 (2020).
120. Westerfield, M. *The zebrafish book 5th edition - A guide for the laboratory use of zebrafish (Danio rerio)*, (University of Oregon Press, Eugene, 2007).

Figure 1

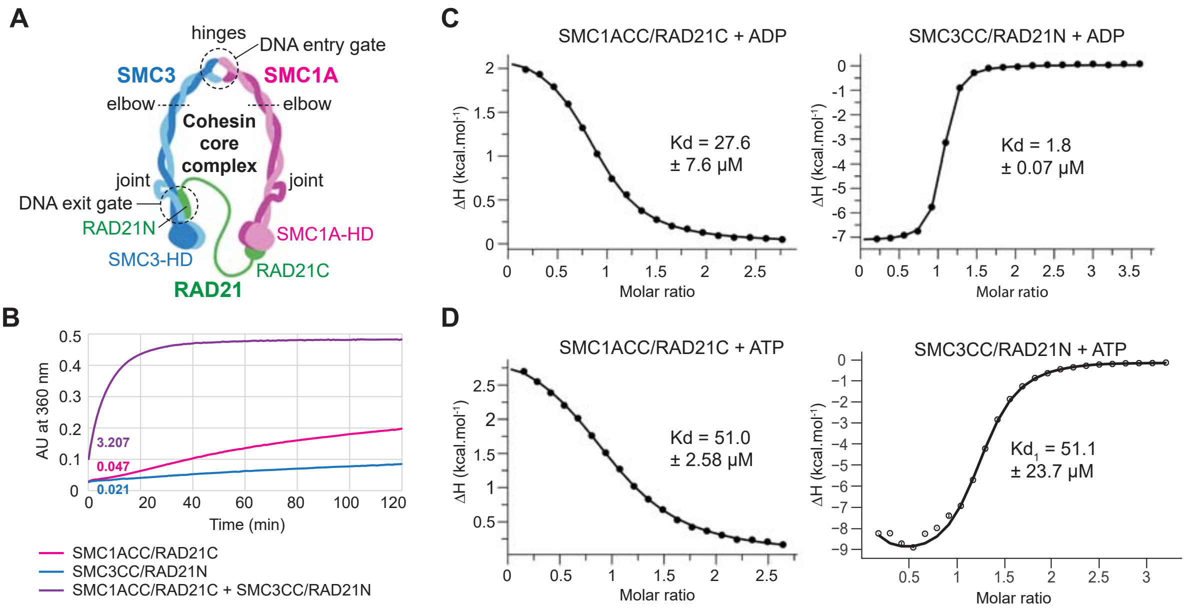
A
hinges
DNA entry gate
SMC3
SMC1A
elbow
elbow
Cohesin core complex
joint
joint
DNA exit gate
RAD21N
SMC1A-HD
SMC3-HD
RAD21C
RAD21
B
AU at 360 nm
0.5
0.4
0.3
0.2
0.1
0
3.207
0.047
0.021
0
20
40
60
80
100
120
Time (min)
SMC1ACC/RAD21C
SMC3CC/RAD21N
SMC1ACC/RAD21C + SMC3CC/RAD21N
C
SMC1ACC/RAD21C + ADP
ΔH (kcal.mol⁻¹)
2
1.5
1
0.5
0
Kd = 27.6
± 7.6 μM
0
0.5
1
1.5
2
2.5
Molar ratio
SMC3CC/RAD21N + ADP
ΔH (kcal.mol⁻¹)
0
-1
-2
-3
-4
-5
-6
-7
Kd = 1.8
± 0.07 μM
0
0.5
1
1.5
2
2.5
3
3.5
Molar ratio
D
SMC1ACC/RAD21C + ATP
ΔH (kcal.mol⁻¹)
2.5
2
1.5
1
0.5
Kd = 51.0
± 2.58 μM
0
0.5
1
1.5
2
2.5
Molar ratio
SMC3CC/RAD21N + ATP
ΔH (kcal.mol⁻¹)
0
−1
−2
−3
−4
−5
−6
−7
−8
−9
Kd1 = 51.1
± 23.7 μM
0.5
1
1.5
2
2.5
3
Molar ratio

Figure 2

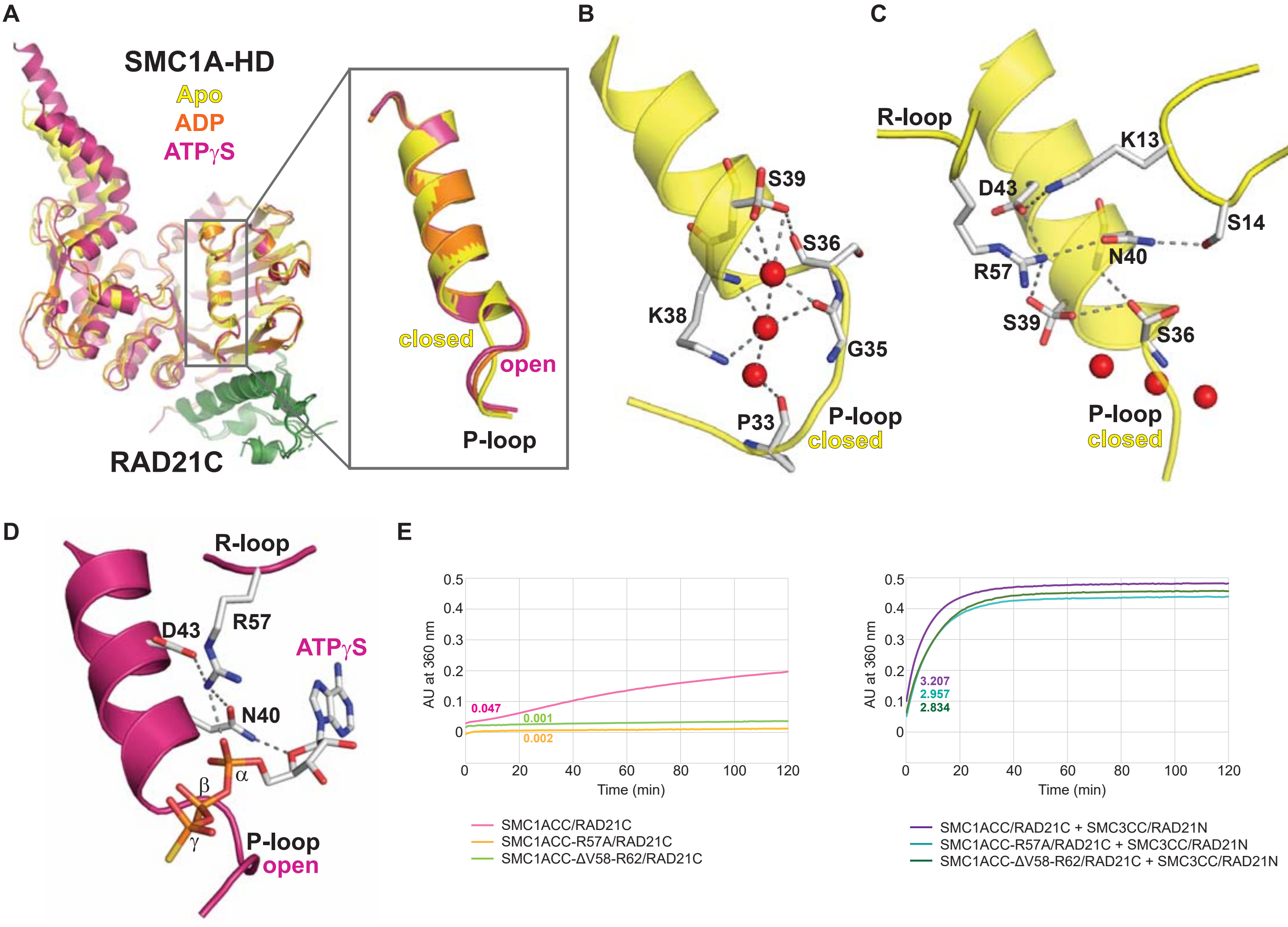
A
SMC1A-HD
Apo
ADP
ATPγS
closed
open
P-loop
RAD21C
B
S39
S36
K38
G35
P33
P-loop
closed
C
R-loop
K13
D43
S14
N40
R57
S39
S36
P-loop
closed
D
R-loop
D43
R57
ATPγS
N40
α
β
γ
P-loop
open
E
AU at 360 nm
0.5
0.4
0.3
0.2
0.1
0
0.047
0.001
0.002
0
20
40
60
80
100
120
Time (min)
SMC1ACC/RAD21C
SMC1ACC-R57A/RAD21C
SMC1ACC-ΔV58-R62/RAD21C
AU at 360 nm
3.207
2.957
2.834
Time (min)
SMC1ACC/RAD21C + SMC3CC/RAD21N
SMC1ACC-R57A/RAD21C + SMC3CC/RAD21N
SMC1ACC-ΔV58-R62/RAD21C + SMC3CC/RAD21N

Figure 3

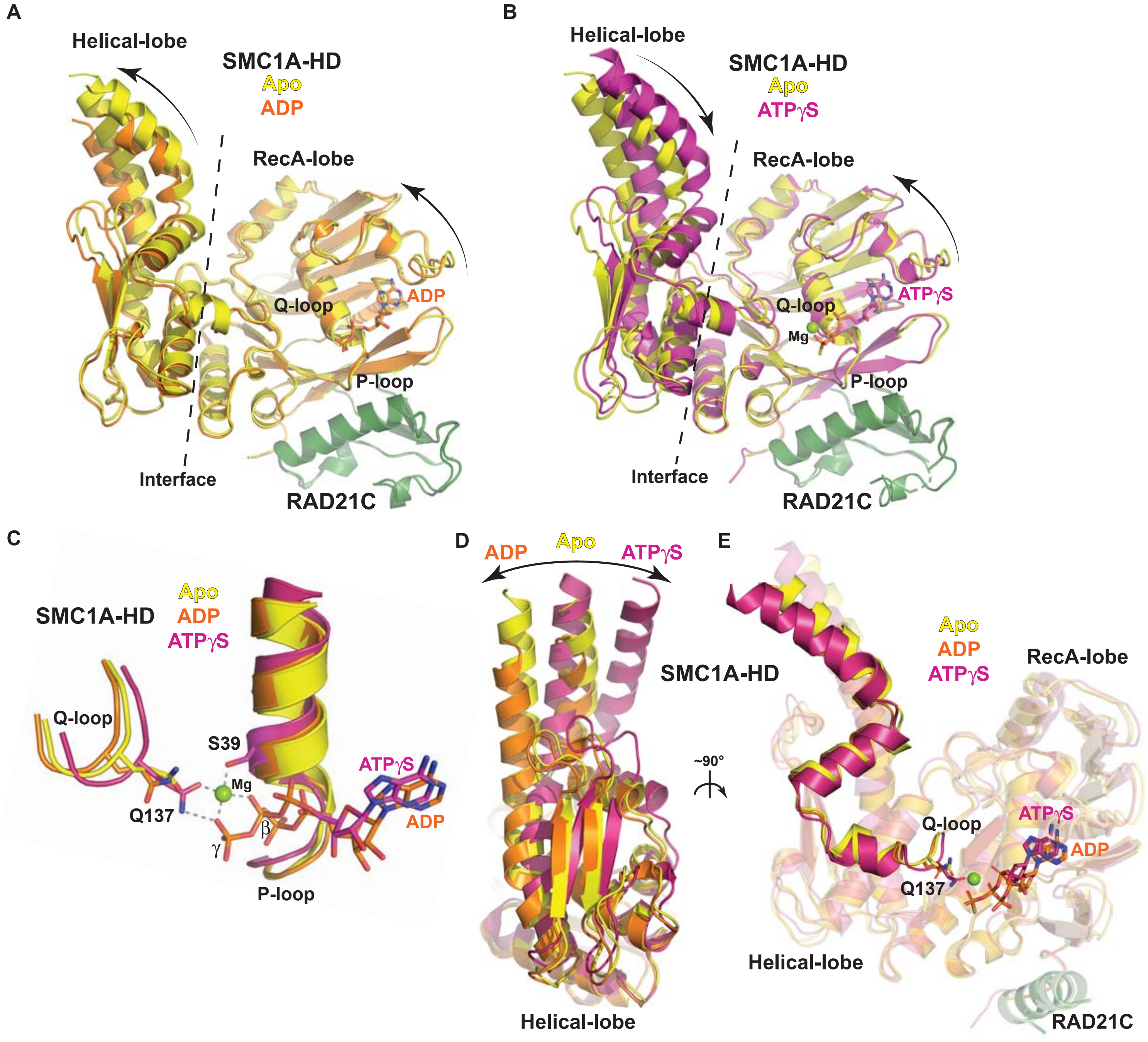
A
Helical-lobe
SMC1A-HD
Apo
ADP
RecA-lobe
Q-loop
ADP
P-loop
Interface
RAD21C
B
Helical-lobe
SMC1A-HD
Apo
ATPγS
RecA-lobe
Q-loop
ATPγS
Mg
P-loop
Interface
RAD21C
C
SMC1A-HD
Apo
ADP
ATPγS
Q-loop
S39
Mg
Q137
β
γ
ATPγS
ADP
P-loop
D
ADP
Apo
ATPγS
SMC1A-HD
Helical-lobe
~90°
E
Apo
ADP
ATPγS
RecA-lobe
Q-loop
ATPγS
ADP
Q137
Helical-lobe
RAD21C

Figure 4

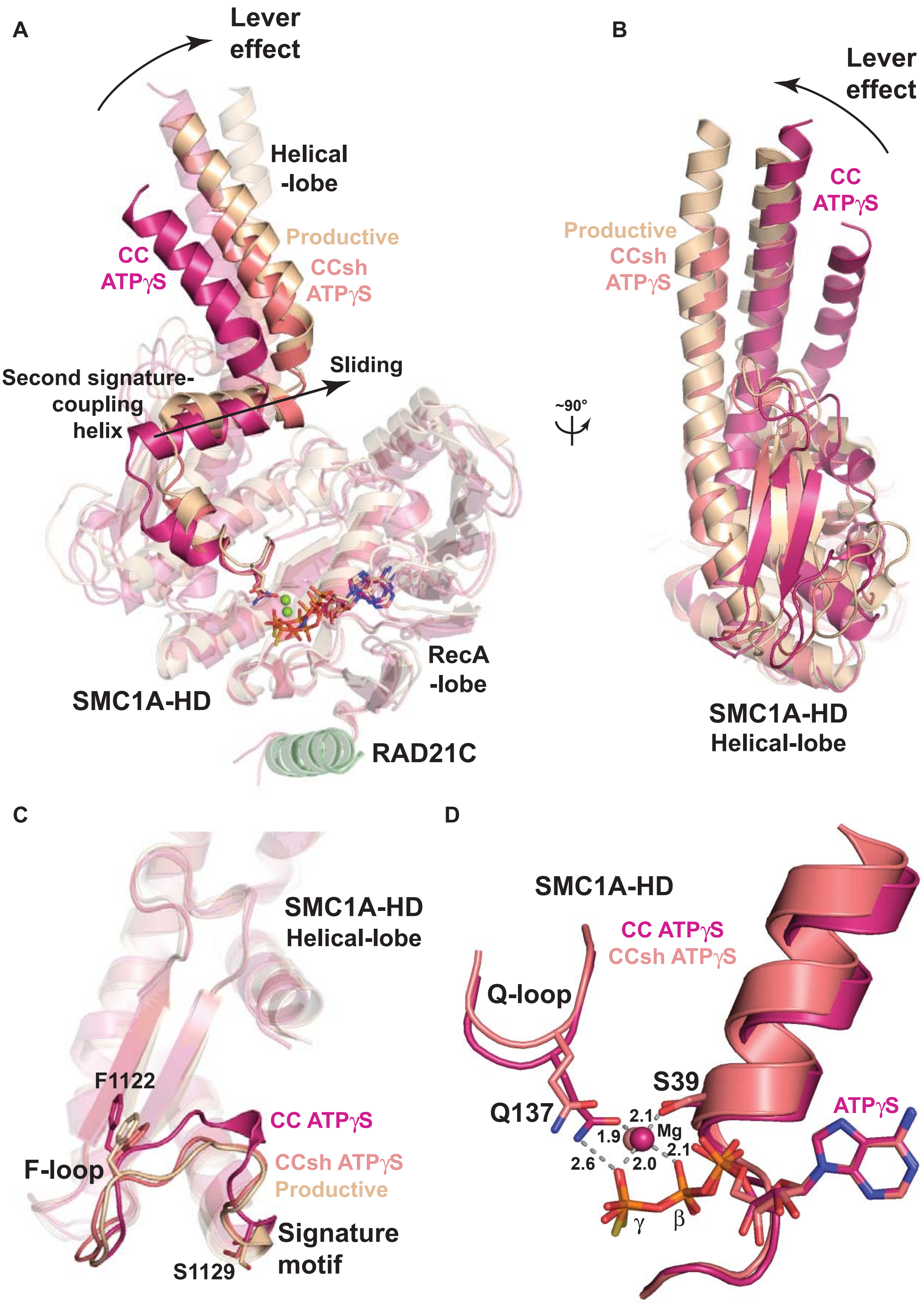
A
Lever effect
Helical -lobe
CC ATPγS
Productive
CCsh ATPγS
Second signature-coupling helix
Sliding
RecA -lobe
SMC1A-HD
RAD21C
~90°
B
Lever effect
CC ATPγS
Productive
CCsh ATPγS
SMC1A-HD Helical-lobe
C
SMC1A-HD Helical-lobe
F1122
CC ATPγS
F-loop
CCsh ATPγS
Productive
Signature motif
S1129
D
SMC1A-HD
CC ATPγS
CCsh ATPγS
Q-loop
S39
Q137
2.1
1.9
Mg
2.6
2.0
2.1
ATPγS
γ
β

Figure 5

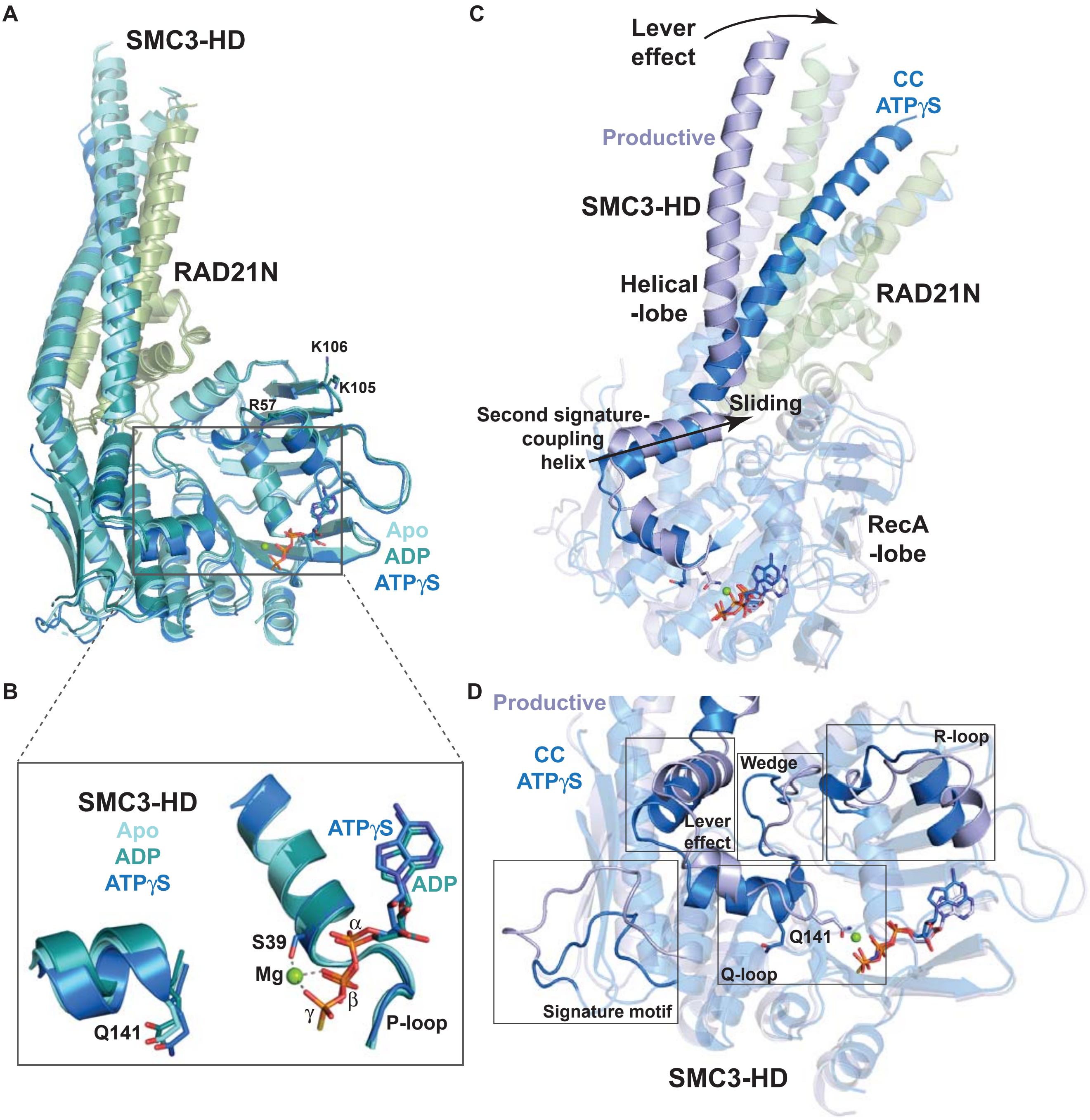
A
SMC3-HD
RAD21N
K106
K105
R57
Apo
ADP
ATPγS
B
SMC3-HD
Apo
ADP
ATPγS
Q141
ATPγS
ADP
S39
Mg
α
β
γ
P-loop
C
Lever
effect
CC
ATPγS
Productive
SMC3-HD
Helical
-lobe
RAD21N
Sliding
Second signature-
coupling
helix
RecA
-lobe
D
Productive
CC
ATPγS
Lever
effect
Wedge
R-loop
Q141
Q-loop
Signature motif
SMC3-HD

Figure 6

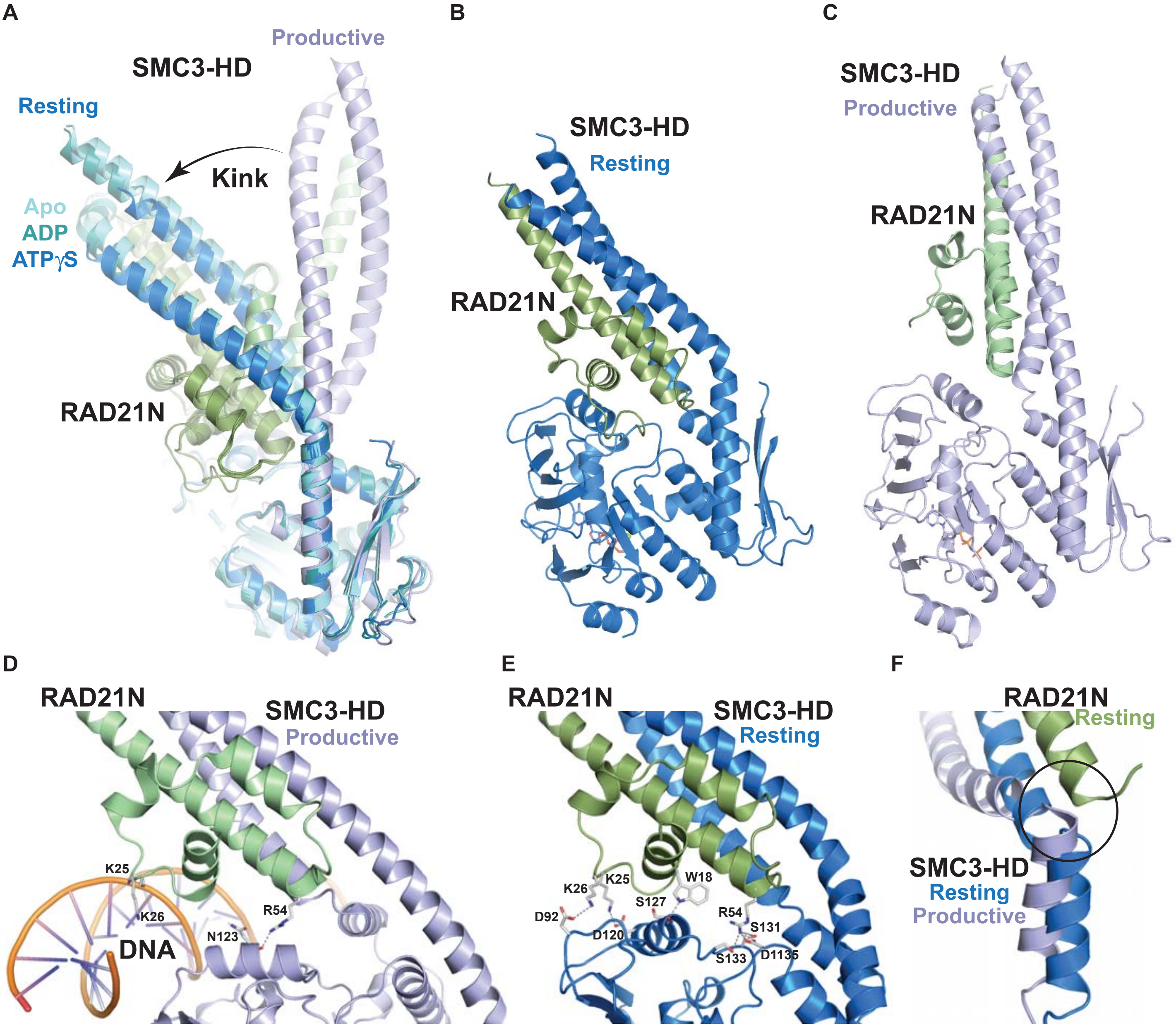
A
Productive
SMC3-HD
Resting
Kink
Apo
ADP
ATPγS
RAD21N
B
SMC3-HD
Resting
RAD21N
C
SMC3-HD
Productive
RAD21N
D
RAD21N
SMC3-HD
Productive
K25
K26
R54
N123
DNA
E
RAD21N
SMC3-HD
Resting
K26
K25
W18
D92
S127
D120
R54
S131
S133
D1135
F
RAD21N
Resting
SMC3-HD
Resting
Productive

Figure 7

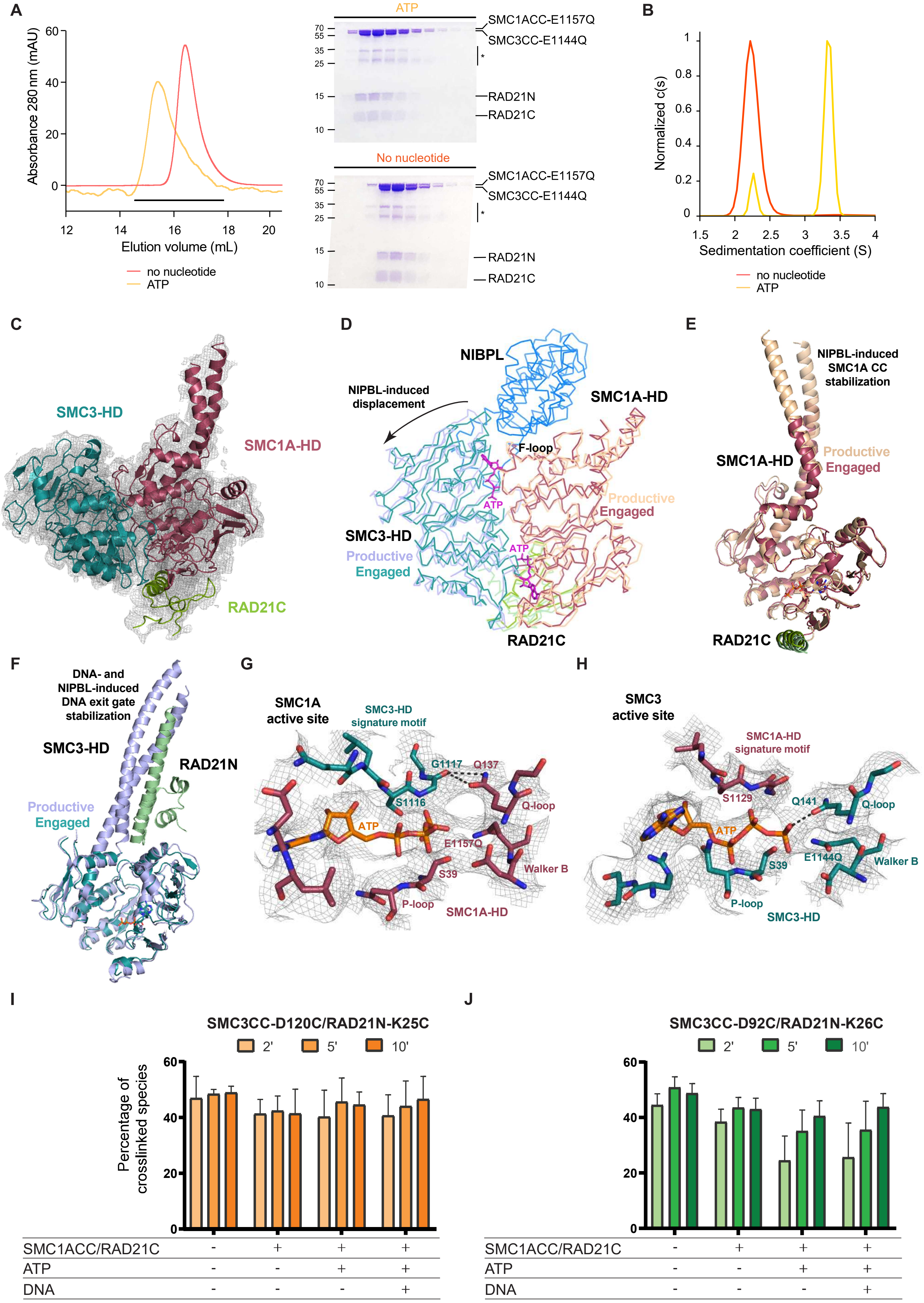
A
Absorbance 280 nm (mAU)
60
40
20
0
12
14
16
18
20
Elution volume (mL)
no nucleotide
ATP
ATP
70
55
35
25
15
10
SMC1ACC-E1157Q
SMC3CC-E1144Q
*
RAD21N
RAD21C
No nucleotide
70
55
35
25
15
10
SMC1ACC-E1157Q
SMC3CC-E1144Q
*
RAD21N
RAD21C
B
Normalized c(s)
1
0.8
0.6
0.4
0.2
0
1.5
2
2.5
3
3.5
4
Sedimentation coefficient (S)
no nucleotide
ATP
C
SMC3-HD
SMC1A-HD
RAD21C
D
NIBPL
NIPBL-induced displacement
SMC1A-HD
F-loop
ATP
Productive
Engaged
SMC3-HD
Productive
Engaged
ATP
RAD21C
E
NIPBL-induced SMC1A CC stabilization
SMC1A-HD
Productive
Engaged
RAD21C
F
DNA- and NIPBL-induced DNA exit gate stabilization
SMC3-HD
RAD21N
Productive
Engaged
G
SMC1A active site
SMC3-HD signature motif
G1117
Q137
S1116
Q-loop
ATP
E1157Q
S39
Walker B
P-loop
SMC1A-HD
H
SMC3 active site
SMC1A-HD signature motif
S1129
Q141
Q-loop
ATP
E1144Q
S39
Walker B
P-loop
SMC3-HD
I
SMC3CC-D120C/RAD21N-K25C
2'
5'
10'
Percentage of crosslinked species
60
40
20
0
SMC1ACC/RAD21C - + + +
ATP - - + +
DNA - - - +
J
SMC3CC-D92C/RAD21N-K26C
2'
5'
10'
60
40
20
0
SMC1ACC/RAD21C - + + +
ATP - - + +
DNA - - - +

Figure 8

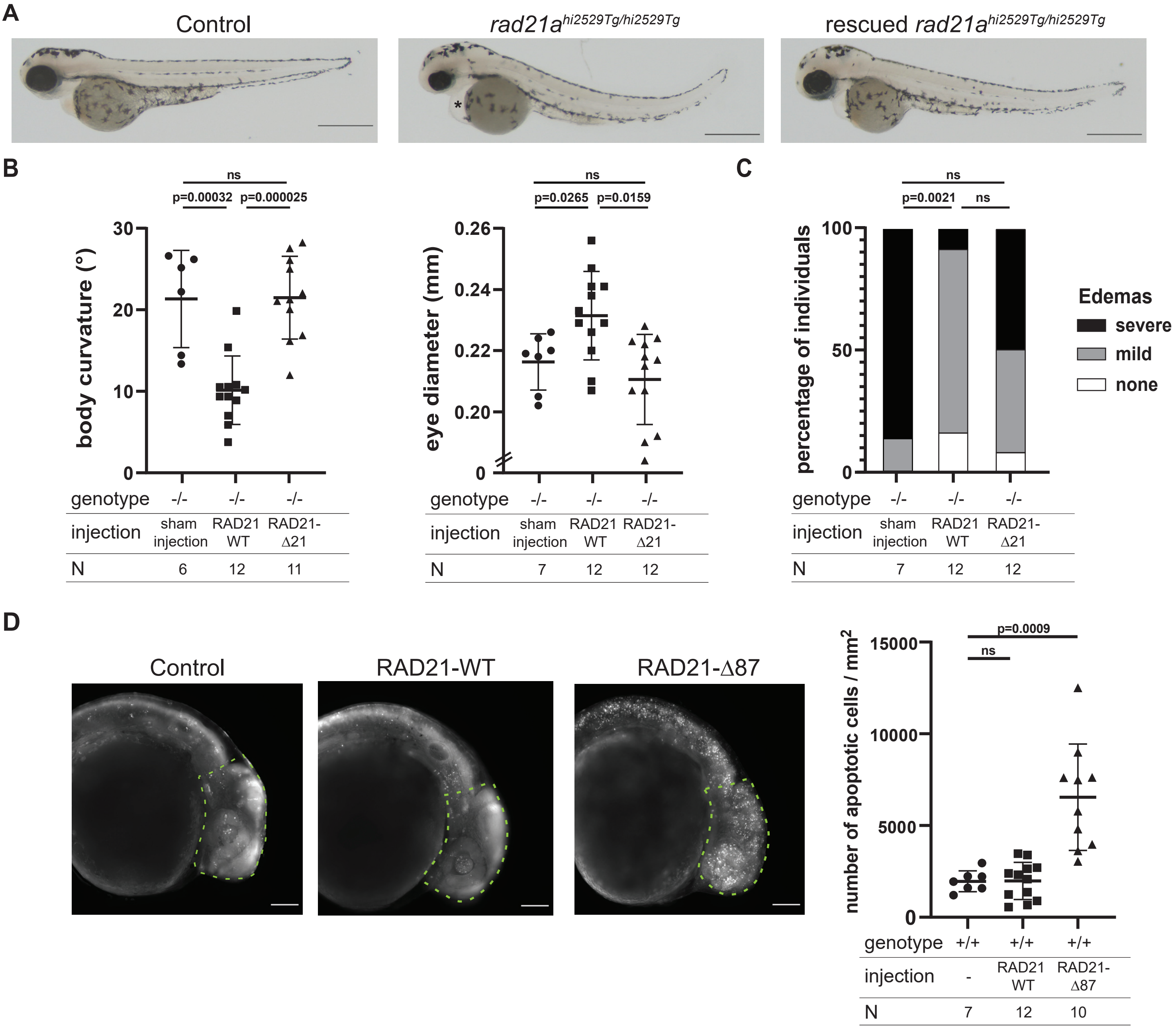
A
Control
rad21a$^{hi2529Tg/hi2529Tg}$
*
rescued rad21a$^{hi2529Tg/hi2529Tg}$
B
ns
p=0.00032
p=0.000025
body curvature (°)
30
20
10
0
genotype -/- -/- -/-
injection sham injection RAD21 WT RAD21-Δ21
N 6 12 11
ns
p=0.0265
p=0.0159
eye diameter (mm)
0.26
0.24
0.22
0.20
0
genotype -/- -/- -/-
injection sham injection RAD21 WT RAD21-Δ21
N 7 12 12
C
ns
p=0.0021
ns
percentage of individuals
100
50
0
Edemas
severe
mild
none
genotype -/- -/- -/-
injection sham injection RAD21 WT RAD21-Δ21
N 7 12 12
D
Control
RAD21-WT
RAD21-Δ87
p=0.0009
ns
number of apoptotic cells / mm^2
15000
10000
5000
0
genotype +/+ +/+ +/+
injection - RAD21 WT RAD21-Δ87
N 7 12 10

Figure 9

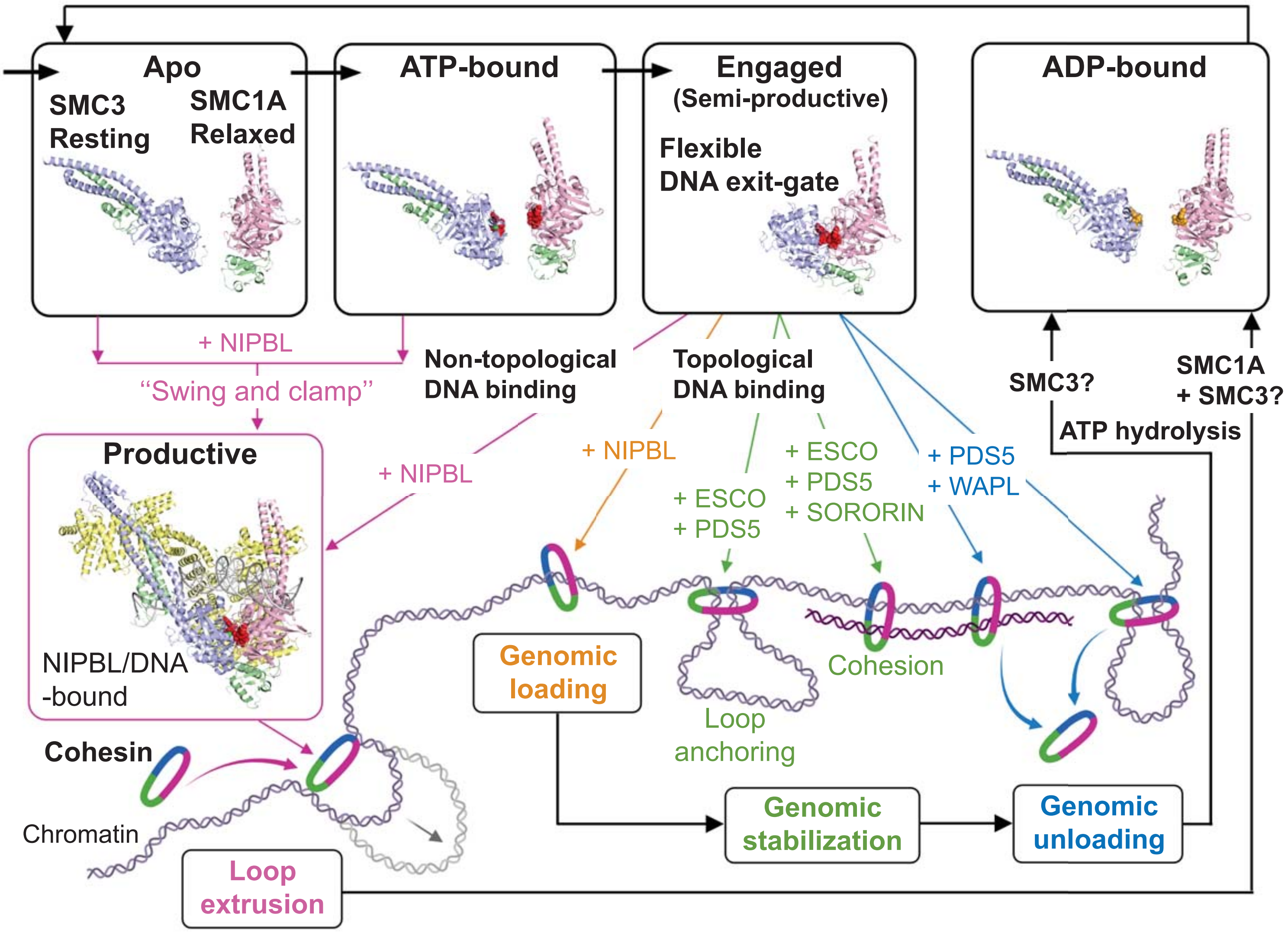
Apo
SMC3
Resting
SMC1A
Relaxed
ATP-bound
Engaged
(Semi-productive)
Flexible
DNA exit-gate
ADP-bound
+ NIPBL
"Swing and clamp"
Non-topological
DNA binding
Topological
DNA binding
SMC3?
SMC1A
+ SMC3?
ATP hydrolysis
Productive
+ NIPBL
+ NIPBL
+ ESCO
+ PDS5
+ ESCO
+ PDS5
+ SORORIN
+ PDS5
+ WAPL
NIPBL/DNA
-bound
Genomic
loading
Loop
anchoring
Cohesion
Cohesin
Chromatin
Loop
extrusion
Genomic
stabilization
Genomic
unloading